Title	Infrared Study for Influence of Binarity on the Disk Dispersal of Young Stars
Author(s)	伊藤, 優佑
Citation	大阪大学, 2015, 博士論文
Version Type	VoR
URL	https://doi.org/10.18910/56074
rights	
Note	

A dissertation for the degree of Doctor of Philosophy

Infrared Study for Influence of Binarity on the Disk Dispersal of Young Stars

Yusuke Itoh

Department of Earth and Space Science

Graduate School of Science

Osaka University

November 12, 2015

Abstract

An important problem in Astrophysics is how and where planets form. A "protoplanetary disk" is the the place where planets are born and is the circumstellar structure that forms during star formation. To date, most theoretical and observational investigations have focused on the planetary formation around single stars. However, binary systems are abundant in star-forming regions compared with single stars. Understanding the protoplanetary disk evolution including binary systems will allow testing new planet formation models.

In this dissertation, we examine the infrared excess emission from circumstellar disks in 27 binary systems located in the star-forming regions of Taurus and Ophiuchus by using the $Spitzer$/Infrared Array Camera (IRAC) archival data at 3.6, 4.5, 5.8, and 8.0 μm. We investigate the difference in excess frequency (EF) of each binary component and the dependence of EF on binary separations. The angular (projected) separations of the binaries are greater than $2''(\sim 280$ AU). This allows to spatially resolve the photometry of individual primary and secondary sources. Primary and secondary stars were resolved by point-spread function (PSF) fitting.

The measured occurrences of infrared excess suggest that binarity plays a role in the evolution of circumstellar disks, even at such wide binary separations. Most of the binaries have excess emissions from both circumprimary and circumsecondary disks or show photospheric levels for both components at all four wavelengths of IRAC. On the other hand, four systems ($17^{+11}_{-8}\%$, designated as "mixed systems") exhibit excess emission from a single binary component. This ratio is significantly smaller than that predicted by

i

the random pairing of single stars, suggesting that circumprimary and circumsecondary disks are synchronously dispersed. In addition, the EFs of primary and secondary sources with projected distances of $a_p \simeq 280 - 450$ AU are $100^{+0}_{-17}\%$ and $91^{+8}_{-18}\%$, respectively, and are significantly higher than in single stars ($70 \pm 5\%$).

We built a simple EF distribution model as a function of disk the radius R_{out} to constrain the dependence of EF on R_{out}. Comparisons with observations using the Kolmogorov-Smirnov test suggest that the observations are consistent with the model when the $\mathrm{EF} \simeq 1$ region is at Rout $\sim$30–100 AU. This disk radius is smaller than that typically estimated for single stars. The high EF of circumstellar disks with such radii suggests prolonged lifetime of dust in binary systems, possibly because the size of disks counteracts the mass loss by photoevaporation.

This study offers a new insights to dependence of the EF, which is equivalent to disk frequency, on binary separations. Depending on the binary separation, different disk frequencies should affect the mass of planets. Therefore, these possibilities could be verified by investigating the planet mass dependence on binary separations. If these dependencies are confirmed, then the planet mass dependence on the disk lifetime or size can be constrained.

Contents

List of Figures

List of Tables

Chapter 1

INTRODUCTION

Since 1995, more than 800 extrasolar planets (hereafter, exoplanets or planets) have been detected. In addition, more than 2000 additional candidate objects from the Kepler mission are to be affirmed (Batalha et al. 2012). Recently, Earth-like planets with mass and size similar to Earth were found within the habitable zone. Earth-like planets were detected in the Gl 581 system, which is in the habitable zone of the star (Udry et. al. 2007, Wordsworth et al. 2010). GJ 1214 is also as a planet located within the habitable zone (e.g., Charbonneau et al. 2009). The place where planets are born is the "protoplanetary disk". Investigating the composition and distributions of temperature, pressure, and density in the disks might help us understand how planets form. In the next section, we discuss the protoplanetary disks.

In this chapter, we introduce theoretical and observational sturdies of protoplanetary disks, planet formation, and binary systems. Next, we describe the aims and approach of this study.

1.1 Protoplanetary Disks

1.1.1 Formation Process of Protoplanetary Disks

At the early stage of star formation, a collapsing molecular cloud core forms a protostar. As accretion proceeds, the envelope becomes tenuous because of rotation and forms a disk-like structure called a protoplanetary disk or hereafter referred to as a "disk"). Most of material which accretes onto the protostar is processed through the accretion disk. In that sense, the formation of protoplanetary disks is therefore a part of a growing up process of the central star. Figure 1.1 shows a schematic of the star and disk formation process. At the youngest protostellar stage ($\sim 10^4$ yrs), called Class 0, the central object is surrounded by a dense envelope. As accretion proceeds, the envelope becomes tenuous and forms a disk. This late accretion phase is called the Class I ($\sim 10^5$ yrs) stage. When the envelope is exhausted, the disk becomes optically visible. This is the classical T Tauri stage (CTTS) and is the Class II ($\sim 10^6$ yrs) stage. Eventually, this protoplanetary disk disappears and becomes a diskless star called the weak-line T Tauri star (WTTS). This is the Class III stage ($\sim 10^7$ yrs).

1.1.2 Observable Signatures of Protoplanetary Disks

The observational methods of protoplanetary disks are described below. The protoplanetary disks initially consist of $\sim$99% *gas* and $\sim$1% *dust* (e.g., Hayashi 1981). The existence of circumstellar disks around young stars has been confirmed based on the emission of gas and dust. Dust amounts to $\sim$1% of the total mass of circumstellar disks. This small amount of dust predominantly controls the disk temperature owing to its high opacity. Optically thick but physically thin dusty disks around stars reprocess the stellar flux and reradiate at wavelengths longer than $\sim$1 μm. The equilibrium temperature of dust may decrease moving away from the center. Hence, the inner disk near the central star radiates at shorter wavelengths, whereas the outside of the disk radiates at longer wavelengths. To
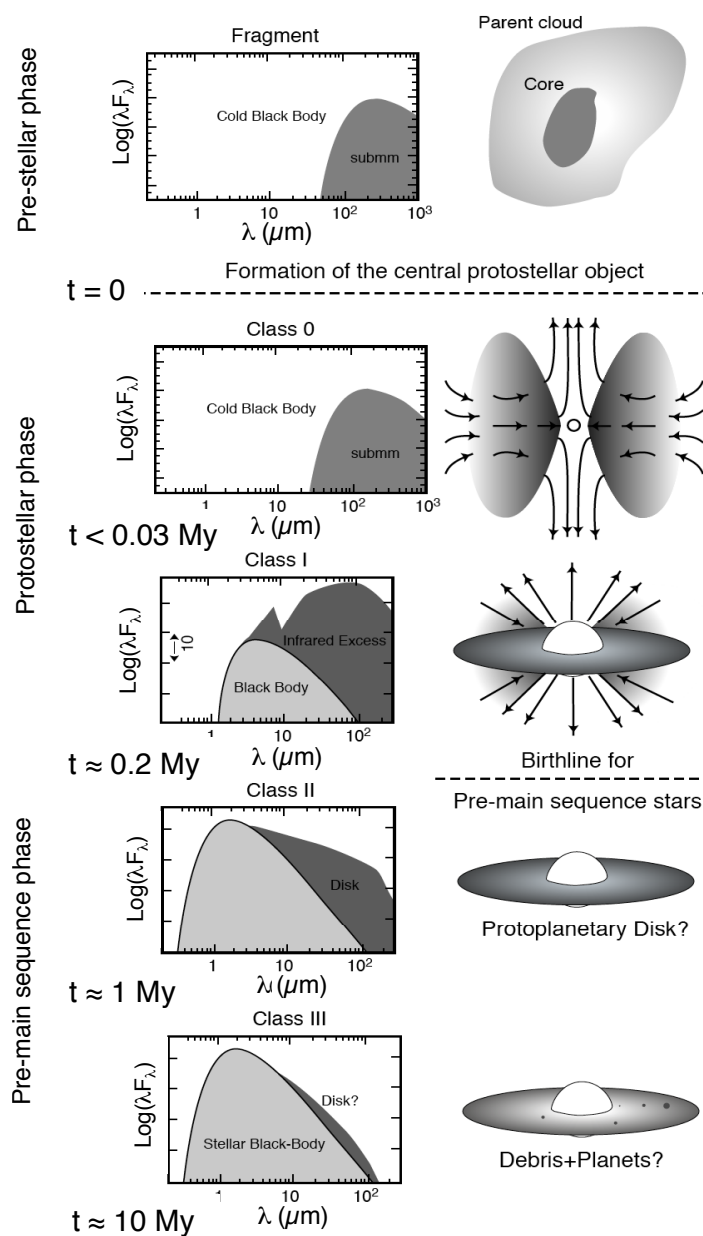
Figure 1.1: Schematic view of star formation. (Nicolas D. Marc C. Annu. Rev. Earth Planet. Sci. 2011, 39, 351)

the degree that the flux at each wavelength exceeds the corresponding blackbody radiation (the temperature of the stellar photosphere), the star is said to have an "infrared excess". We can see the infrared excess emission from irradiated dust in the spectral energy distribution (SED). Figure 1.2 shows the schematic of the SED exhibiting infrared excess. The initial massive disk gradually decreases owing to mass-loss mechanisms; therefore, infrared excess decreases with proceeding of mass-loss evolution. Historically, based on the slope α of the infrared SED, the evolution of disks is classified into three groups (Lada 1987). The slope is between 2 and 25 μm. For the K (2.2 μm) and N (10 μm) bands, $\alpha > 0$, $-1.5 < \alpha < 0$, and $\alpha < -1.5$ correspond to Class I, II, and III, respectively.
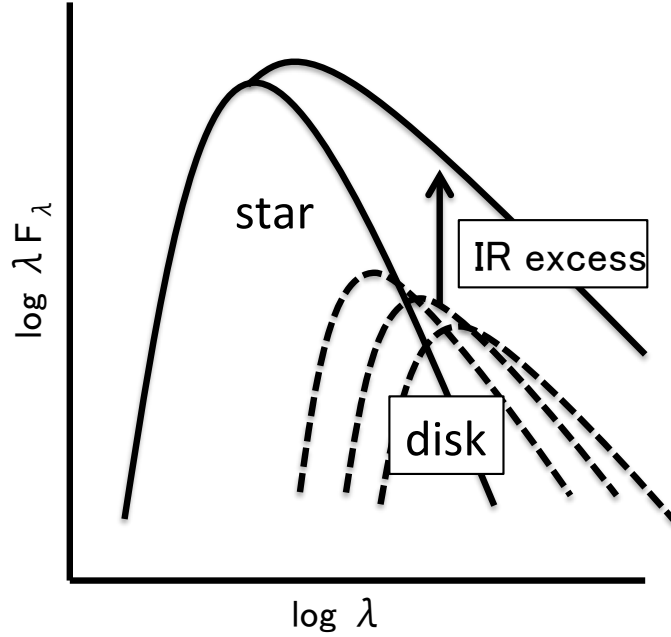
Figure 1.2: Schematic depiction of the SED of a young star surrounded by a disk. The presence of the disk is inferred from the infrared excess (above the expected photospheric value) at wavelengths longward of $\sim$1 μm.

The signature of gas accretion implies the existence of disk and is used to distinguish the different evolution phases based on the equivalent width of the Hα emission. In the initial stage of disk evolution, the star surrounded by the active accretion disk yields a wide equivalent width of Hα emission (CTTS). On the other hand, when accretion ceases and the deprives of such disks, the star represents a more advanced evolutionary stage

(WTTS).

1.1.3   Disk Evolution: Observations and Theory

The interpretation of the physical processes that drive the evolution of disks is critical to understand of planet formation. In this section, we discuss models and observations regarding the evolution of circumstellar disks. Mass is the key parameter associated with disks. The disk mass is determined by sub- or millimeter wavelength observations of dust. Beckwith et al. (1990) and Andre & Montmerle (1994) were the first large millimeter surveys that measured disk masses at 1.3 mm in the Taurus-Auriga and Ophiuchus star-forming regions. Both regions comprise low mass stars, $M_* < 1 M_{sum}$ ($M_{sun} = 1.989 \times 10^{33}$ g), which mostly belong to the K–M spectral types. Andrews & Williams (2005, 2007a) showed that the median mass of Class II young-stellar object (YSO) disks is $5 M_{Jup}$ and the median ratio of the disk to stellar mass is ∼1%. Based on previous studies, most disks are only a small percentage of the stellar mass. The disk size R_c is also an important parameter and is commonly determined in terms of an intensity threshold because the disk does not have a clear outer edge. Hughes et al. (2008) determined $R_c = 30$–200 AU for four disks by fitting the exponentially tapered profile. Similar sizes of disks were reported in Taurus-Auriga ($R_c \simeq 30$–230 AU; Isella, Carpenter & Sargent 2009) and Ophiuchus ($R_c = 14$–198 AU; Andrews et al. 2009, 2010b) star-forming regions. Because the outer parts of their disks are cool and emit weakly, estimates of the disk sizes have large uncertainties.

One of the principal parameters of disk evolution is the disk lifetimes because it limits the time available for planet formation. The measurements of near-infrared excess in nearby star-forming regions suggest that 60–80% of stars (¡ 1 Myr) have measurable excesses (e.g., Strom et al. 1989). The near-infrared excess only traces the inner region of the disk. The decrease of sources showing near-infrared excess has been modeled as an exponential function with a time constant of 2.5 Myr (see Figure 1.3; Mamajek 2009).
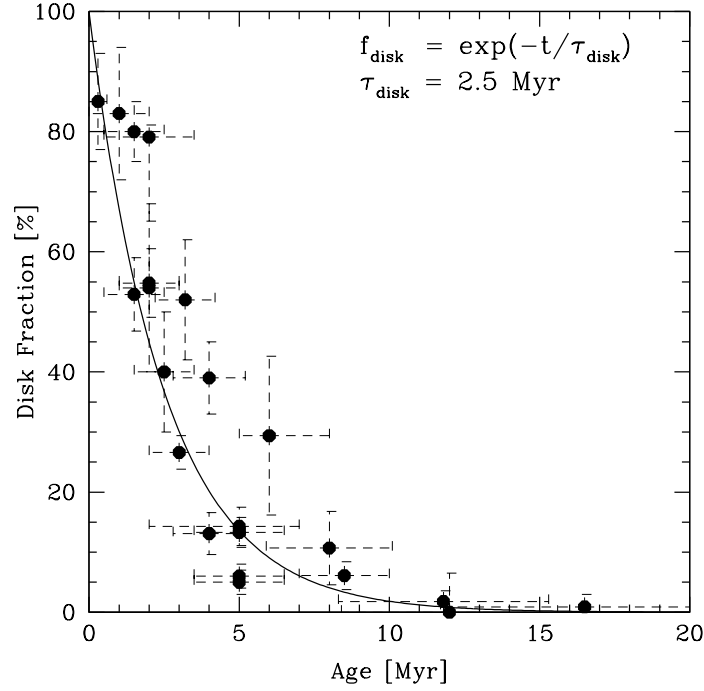
Figure 1.3: Age of stellar sample vs. fraction of stars with primordial disks (the "Haisch-Lada2" plot) either through Hα emission or infrared excess diagnostics (Mamajek 2009).

The timescale of the dissipation in the outer disk can be investigated by observing the fraction of stars with mid-infrared excesses in nearby star-forming regions with different ages. A near- to mid-infrared survey (3.6 to 24 μm) using the *Spitzer Space Telescope* provide a wealth of data to derive the dissipation timescale of disks. The project "From Molecular Cores to Planet-forming Disks" (c2d) (Cieza et al. 2007, Padgett et al. 2006, Wahhaj et al. 2010) showed that $\sim$80% of WTTS have 24 μm fluxes correspond to stellar photospheres. This means that once accretion stops and the inner disk disperse, the outer disk also disperses quickly. In addition, $\sim$50% of the WTTS younger than 1–2 Myr do not have a disk and the time constant corresponds to $\sim$1 Myr. The c2d also suggests that $\sim$10 Myr is the upper limit for disk lifetime around solar-type stars.

A small population of stars exists that lacks near-infrared excess but still exhibits strong dust emission at longer wavelengths; these stars, the so-called "transitional disks", are considered to have an inner hole in their disks. In addition, the observations suggest that few stars without near-IR excess show mid-IR excess emission. This implies that once

the inner disk dissipates, the outer disk disappears very rapidly. These disks constitute 20% of the disk population (Cieza et al. 2009, Dahm & Carpenter 2009, Fang et al. 2009) at most. From the above arguments, the dissipation timescale of the entire disk has been estimated at $\lesssim$0.5 Myr (e.g., Cieza et al. 2007, Skrutskie et al. 1990, Wolk & Walter 1996). Considering the lifetime of disks for objects located nearby star-forming regions ($\sim$2.5 Myr), the dissipation timescale of the entire disk is short an it is known as the two-time-scale problem. The combination of the viscous and photoevaporation mechanism described below is a successful model.

Viscous Model   The viscous evolution model is broadly consistent with the observations, such as disk sizes and the decrease in the accretion rate (Hartmann et al. 1998, Hueso & Guillot 2005). The viscous dissipation is attributed to the viscosity of the gas, which causes the angular momentum transportation and the movement of the gas from the outside to the inside. Finally, the accretion to the star takes place. The self similar solution for the evolution of a viscous model predicts that the surface density and accretion rate of the disk decrease according to a power-law; hence, the transition between the disk and disk-less states is gradual. However, this is not observed; the viscous evolution model fails to explain the variety of observed SEDs. In addition, this model cannot explain the SEDs for relatively small number of objects without inner disks but with outer disk (transitional disks).

Photoevaporation Model   Photoevaporation depends on the gas in the disk that is ionized by ultraviolet radiation from the central star. If the kinetic energy of the ionized gas is larger than the gravitational potential, the ionized gas dissipates. The gravitational radius is $R_g = GM_*/a^2$ (e.g., Hillenbach et al. 1994), where a is the sound speed. In the early stage of disk evolution with active accretion, a hole does not form even in areas where photoevaporation is effective near R_g. However, rapid removal of the material occurs because the supply from the outside decreases with time. Therefore, the probabil-

ity that this evolution stage can be observed is very small, and the disk with or without a hole can be observed. According to Clarke et al. (2001), this time scale is 10^5 yrs with $1M_{sun}$. Figure 1.4 (*left*) shows snapshots of the surface density profile based on the viscous accretion model, whereas Figure 1.4 (*right*) shows a corresponding model with photoevaporative mass loss for comparison.
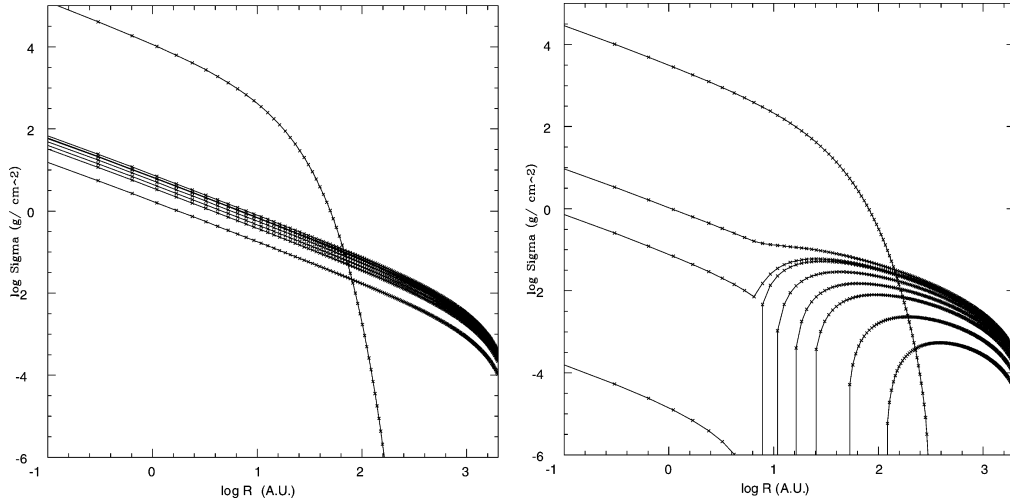
Figure 1.4: Snapshots of the surface density distribution in the disk as per the viscous accretion model with photoevaporative mass loss (*left*) and without photoevaporative mass loss (*right*) Clarke et al. (2001). The reach curves represent $t = 0, 1.3 \times 10^7, 1.41 \times 10^7, 1.43 \times 10^7, 1.6 \times 10^7, 1.8 \times 10^7, 2.0 \times 10^7, 2.4 \times 10^7, and 2.8 \times 10^7$ yr from the top to bottom. The dramatic decrease in the inner disk with photoevaporative mass loss only over the 2×10^5 yr.

1.1.4 Planet Formation

There are two well known planet formation mechanisms: (1) core accretion, in which particles form kilometer-sized planetesimals that eventually grow to form planetary cores (Wetherill 1990, Pollack et al. 1996), and (2) gravitational instability, in which part of the massive disk quickly forms giant planets via self-gravity (Toomre 1964, Boss 1997, 2000).

Observational studies have shown that about half of the stars in young clusters lose their disks within ~3 Myr (Haisch et al. 2001, Mamajek 2009). Core accretion is mech-

anism that is difficult to contribute to the formation of Earth-like planets before disk dispersal occurs within the estimated disk lifetime of a few million years. In addition, the mechanism for the coupling of meter-sized particles is poorly understood. On the other hand, gravitational instabilities could form planets fast; thus, this mechanism is able to avoid the timescale problem. However, the instabilities require high densities. The disk lifetime is an effective parameter in evaluating the validity of planet formation models theoretically.

1.2 Binary Systems

In the previous section, we discussed star formation and protoplanetary disks in the case of a single star. Most planets that have been discovered to date exist around single stars as in our solar system. On the other hand, it is well known that many stars in young star-forming regions at the solar system neighborhood are in binary or multiple systems. More than 60% of solar-type stars in the main-sequence (e.g., Abt & Levy 1976; Duquennoy & Mayor 1991) and 35–43% of M-type stars are in binary or multiple systems(e.g., Fischer & Marcy 1992; Delfosse et al. 2004). Numerous young binaries have also been detected in nearby star-forming regions (e.g., Ghez et al. 1993; Simon et al. 1993). Therefore, this suggests that the number of planets discovered in binary systems is lesser than the number around single stars. Considering the high frequency of multiple systems, the relation between disks and binary companions must be obtained to fully understand the disk evolution and planet formation. In this section, we discuss binary systems and their protoplanetary disks.

1.2.1 Theory for Binary Formation

Different formation models for binaries exist. The models have been divided into capture and fragmentation scenarios. Capture refers to the tidal capture of two unbound objects (e.g., McDonald&Clarke 1993). For each primary star, the mass of the secondary star is selected randomly from the single star. However, tidal capture might be too inefficient to produce high binary fractions.

Fragmentation models are classified as prompt fragmentation (e.g., Boss 1986; Bonnell & Bastien 1992) and disk fragmentation (e.g., Bonnell 1994; Stamatellos & Whitworth 2009). In the prompt fragmentation scenario, both primary and secondary stars form in the same collapsing molecular cloud. In the disk fragmentation scenario, secondary stars form within the circumprimary disks via density perturbations.

In binary formation models, mass ratio is one of the most important parameter. In the

prompt fragmentation model, the continued accretion from the in-falling gaseous envelope considers masses of both components, e.g., the same degree of accretion equalizes both masses. In general, the accretion of gas with low specific angular momentum increases the difference of stellar masses, whereas the accretion of gas with high specific angular momentum drives the mass ratio toward unity(Artymowicz 1983, Bate 1997, Bate & Bonnell 1997, Bate 2000).

1.2.2 Theory for Disk Truncation

In binary systems, two types of disks are present. One surrounds each component, and the other is for both components and is centered at the common center of mass. Numerical simulations of circumstellar material within a binary suggest that "circumprimary" and "circumsecondary" disks are possible as well as "circumbinary" disks (Artymowicz & Lubow 1994; Bate & Bonnell 1997). Based on numerical simulations, the inner disks are expected to be tidally truncated at roughly $1/3$ of the semi-major axis a of the binary (Artymowicz & Lubow 1994). The inner edge of the circumbinary disk expands to $\sim$2–$3a$. Recent semi-analytic approximations for truncated disk size R_{out} used the following expressions (Eggleton et al. 1983; Pichardo et al. 2005; Harris et al. 2012):

$$R_{\mathrm{out}} = 0.337 \left[\frac{(1-e)^{1.2} \phi^{2/3} \mu^{0.07}}{0.6\phi^{2/3} + \ln(1 + \phi^{1/3})} \right] a \qquad (1.1)$$

where e is the eccentricity, $\mu = q/(1+q)$ is the mass fraction of the stellar components, and ϕ is

$$\phi_{\mathrm{pri.}} = m_{\mathrm{pri.}}/m_{\mathrm{sec.}} = \frac{1-q}{q} \text{ and } \phi_{\mathrm{sec.}} = m_{\mathrm{sec.}}/m_{\mathrm{pri.}} = \frac{q}{1-q}. \qquad (1.2)$$

According to the conventional definition, in a binary system of stars, the primary and secondary masses are $m_{\mathrm{pri.}}$ and $m_{\mathrm{sec.}}$ ($m_{\mathrm{pri.}} > m_{\mathrm{sec.}}$), respectively. Based on the above equations, we show R_{out} as a function of the mass ratio and eccentricity in Figure 1.5.

As shown in Figure 1.5, the outer radius of circumstellar disks is truncated at $\sim$30%

(a) Dependence of R_{out} on mass ratio   (b) Dependence of R_{out} on eccentricity
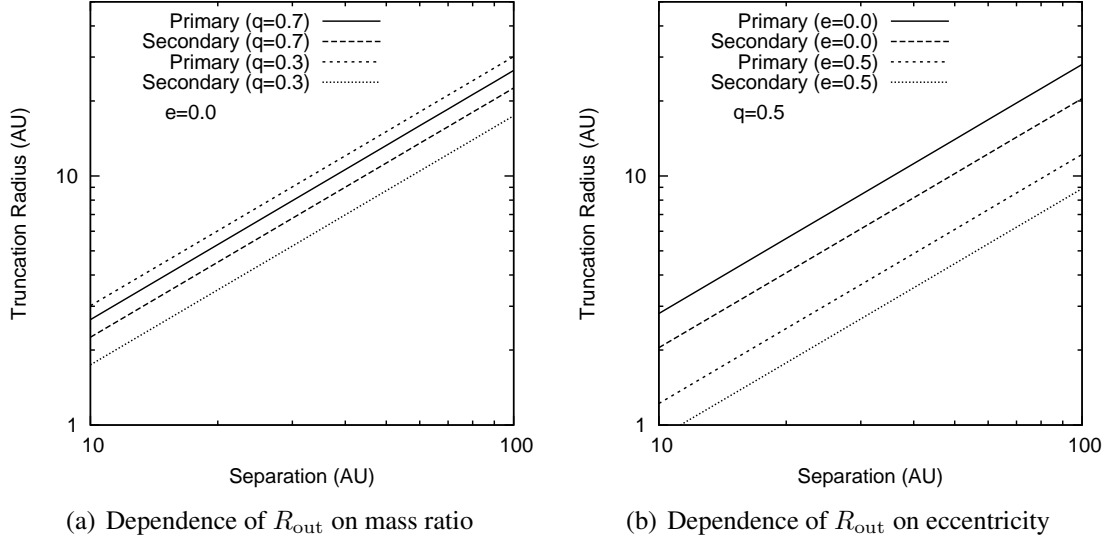
Figure 1.5: Dependence of R_{out} on eccentricity and mass ratio. (a) The truncated radius for both components is shown for $e = 1$. The case of high ($q = 0.7$) and low ($q = 0.3$) mass ratios are shown. The truncated radius for secondary stars coincides with that of the primary star when $q = 1$. (b) The truncated radius of both components is shown for $q = 0.5$. The truncated radius is approximately 30% of the separation for $e = 0$ and decreases with increasing eccentricity. When the eccentricity is 0.5, the truncated radius is $\sim$10% of the separation.

of the separation. The size of circumprimary and circumsecondary disks depends on the stellar mass, with the massive component having a larger size of disk and *vice versa*. High eccentricity implies a more truncated radius with scale in the order of $\sim$10% of the separation. One of the basic mechanisms of disk evolution is the viscous accretion model with an evolution timescale that strongly depends on the disk size. In the case of viscous evolution, the dissipation timescale is $t \propto R_{out}^2$. Considering the relation between the binary separation and its dependence on the disk size, enhanced evolution of the circumstellar disk is predicted for more closed separation. On the contrary, the time to remove the disk might increase with binary separation; hence, the disk size increases. As described in the next section, past studies have shown that the disk frequency of closed binaries with sufficiently truncated disk size is significantly shorter than that of a single star, whereas that of wide binary system corresponds to the disk frequency of single stars.

1.2.3 Previous Study for Binary Systems

Numerous young binaries have also been detected in nearby star-forming regions (e.g., Ghez et al. 1993; Simon et al. 1993). Observational study of young binaries is particularly important for understanding how stars acquire their planetary systems. In early studies, observations of protoplanetary disks have revealed that tight binaries, whose separation is closer than $\sim$40 AU, show substantially reduced (sub)millimeter emission (Beckwith et al. 1990; Jensen et al. 1996). These trends can be interpreted as companion-induced disk truncation which drive the reduced disk mass and outer radius. Several spectroscopic studies have identified circumprimary disk and circumsecondary disk accretion signatures for wide binaries ($\gtrsim$100 AU) (Brandner & Zinnecker 1997; Prato&Simon 1997; Monin, Menard & Duchene 1998; Duchene et al. 1999; White et al. 1999). These proved that both circumprimary and circumsecondary disks can exist at least for wide binary. Circumprimary and circumsecondary disks around SR 24 in Ophiuchus have been directly imaged in the near-infrared region, enabling a detailed comparison with theoretical predictions of disk formation and evolution in binary systems (Artymowicz & Lubow 1994; Mayama et al. 2010). In addition, excess emission in the infrared and millimeter regions has been statistically analyzed to investigate the evolution of circumstellar disks in binaries. Disk evolution in binary systems should depend on binary parameters such as separation and mass ratio. However, the evolutionary process is less clear than in single stars, because sufficient data have not been accumulated.

Nevertheless, consistent results have emerged from previous observational studies on binary properties such as separation and differences in disk frequency between primary and secondary stars. White & Ghez (2001) investigated the nature of circumprimary and circumsecondary disks from their Hα and $K - L$ colors. Because the lifetimes and accretion rates of circumprimary disks exceed those of the secondary disks, they concluded that, in general, most of the material in a circumprimary disk is supplied by the circumbinary disk. Similarly, Monin et al. (2007) used Hα emission, $K - L$, and $K - N$ to inves-

tigate circumstellar disks in binaries. They found that there were fewer systems showing the gas accretion only onto the secondary stars than systems only accreting onto the primary stars. Therefore, they deduced that the lifespan of circumprimary disks exceeds that of circumsecondary disks. Past studies have also revealed how the disk existence depends on binary separation (Prato & Simon 1997; Duchêne et al. 1999; White & Ghez 2001; Hartigan & Kenyon 2003; Daemgen et al. 2012, 2013). Cieza et al. (2009) showed that the lifetime of circumstellar disks in binary systems is significantly shorter (relative to disks surrounding single stars) at separations of 40 AU and below. They investigated infrared excess from binaries in four nearby star-forming regions ($\sim$1–3 Myr) using the $[3.6] - [8.0]$ color obtained by *Spitzer*/IRAC without resolving the individual stellar components (Figure 1.6 *(left)*). Accelerated dispersal of circumstellar disks in close binary systems is also suspected among the members of η Chamaeleon which are aged $\simeq$8 Myr (Bouwman et al. 2006). Similar results have been recently reported by Kraus et al. (2012), who studied excess emission in Taurus binaries over a wide range of wavelengths, from near-infrared to millimeter (Figure 1.6 *(right)*). From these data, they calculated the disk frequency, also without resolving individual stellar components. While $\sim$67% of the close binaries ($\lesssim$40 AU) disperse their disks within $\sim$1 Myr, $\sim$80–90% of single stars and wide binary systems ($\gtrsim$400 AU) retain their disks during $\sim$1–2 Myr. These results can be seen in Figure 1.6 (b). We plot the disk frequency as a function of binary separation divided into different diagnostic observations. Although the disk diagnostics show the different values of disk frequency, there is same behavior that the disk frequency for close ($\lesssim$40 AU) binary systems is lower than that for wider binaries.

Some properties of the circumstellar disks, such as the disk frequency (e.g., Bouwman et al. 2006; Cieza et al. 2009; Kraus et al. 2012), gas accretion, and dust emission (e.g., White & Ghez 2001; Daemgen et al. 2012), have been reported to be indistinguishable between wide binaries and single stars. While many studies indicate accelerated disk dispersal in close binary systems, the dependence of the disk dissipation time scale on wide binary separation ($\gtrsim$100 AU) has been little investigated. Especially, sample

size was insufficient, and binary components were not spatially resolved at mid-infrared wavelengths.
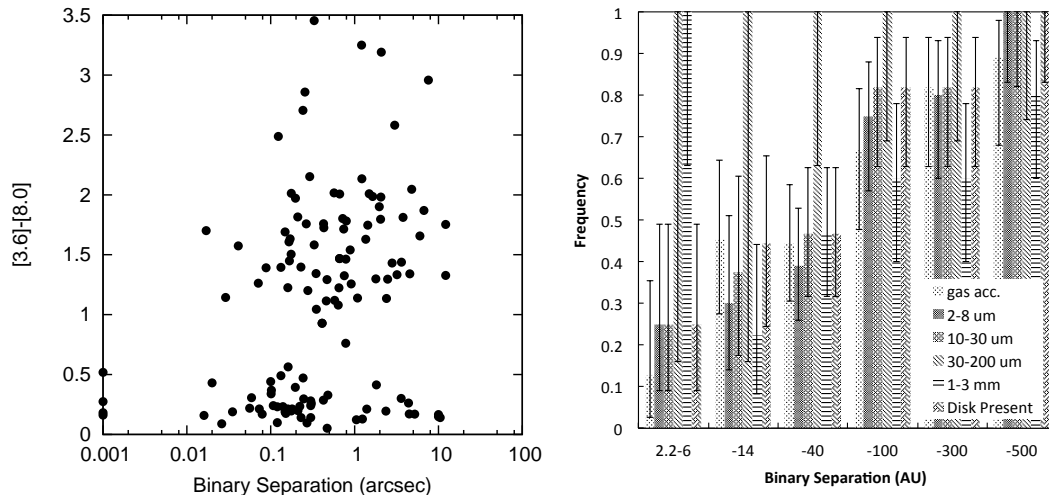
(a) $3.6-8.0$ vs. projected separation for entire sample of Cieza et al. (2009).

(b) Disk frequency as a function of binary-projected separation for in Taurus-Auriga (Kraus et al. 2012).

Figure 1.6: (a) $[3.6]-[8.0]$ vs. binary-projected separation for Cieza et al. (2009) sample. Binary systems with $[3.6]-[8.0]<0.8$ are considered to be diskless, while systems with $[3.6]-[8.0]>0.8$ are considered to have at least one disk. (b) Disk frequency as a function of binary-projected separation for Taurus-Auriga star-forming region. Six ranges of binary separations are shown. The vertical error bars represent the 1σ confidence interval containing the central 68% of the binomial distribution. The disk frequency for closer binaries than 40 AU is significantly lower than that for wider binaries, although depending on the used disk indicator.

1.3   Our Approach

In this thesis, we discuss the infrared emission from *each* stellar component of binary systems. The analysis is based on spatially resolved photometry at four wavelengths (3.6, 4.5, 5.8, and 8.0 μm) obtained from *Spitzer*/IRAC images. The wavelengths of the Infrared Array Camera (IRAC) correspond to dust temperatures of $\sim$360–800 K and a radial region within a few AU for M-type stars. Thus, these wavelengths can probe the inner planet-forming radii in dusty disks. In addition, the *Spitzer*/IRAC bands located between L and N are difficult to access with ground-based telescopes; therefore, new data, such as the onset of infrared excess emissions can be obtained. Moreover, the unprecedented sensitivity of *Spitzer* enables the detection of lower mass secondaries. We sampled binary systems with projected separation ap of $2\rlap{.}''0$–$17\rlap{.}''0$, corresponding to $\sim$300–2400 AU at 140 pc. Because the images of the primary and secondary stars overlap at the projected separations near $2''$, we analyzed each star by stellar profile fitting photometry.

Chapter 2

Study of Infrared Excess from Circumstellar Disks in Binaries with *Spitzer*/IRAC

2.1 Our Binary Sample and Archival Data

2.1.1 *Spitzer Space Telescope* **and Archival Data**

Spitzer is infrared telescope launched in 2003. The instruments, IRAC, IRS, and MIPS
are equipped (Fazio, G. et al. 2004). IRAC provides simultaneous 5.2×5.2 arc minutes
images at 3.6 ,4.5, 5.8 and 8.0 μm and each wavelength is called as 1ch, 2ch, 3ch and
4ch, respectively. IRS is a spectrometer that gives spectrum in the range of 5.2–38 μm.
MIPS has capability of taking images at in 24, 70, and 160 μm. The diameter of the
primary mirror (D) is 85 cm, which provide diffraction-limited resolution ($\theta = 1.22\lambda/D$)
of $\sim 2\rlap{.}''0$ at the wavelengths for IRAC. The atmosphere influences the infrared observation
for ground-based observations though space satellite such as Spitzer can observe without
the influences of atmosphere, thus *Spitzer* has unprecedented sensitivity. In this thesis,
archival data obtained by *Spitzer* telescope are used. Sometimes, there are objects ob-
served many times by different projects, and each dataset can be downloaded as raw data
or calibrated data.

2.1.2 Binary Sample

The full-width at half-maximum (FWHM) of a point source is $2''$ at 8.0 μm for *Spitzer*/IRAC
(Fazio et al. 2004). Given the array pixel scale of $1\rlap{.}''2$, we selected binary systems with
projected separations greater than $2\rlap{.}''0$. Thirty-three binaries of separation of $1\rlap{.}''95$–$17\rlap{.}''0$
in the star-forming regions of Taurus (distance 140 pc; Torres et al. (2007), age 1–2 Myr;
Kraus & Hillenbrand (2009a)) and Ophiuchus (distance 140 pc; Loinard et al. (2008), age
1 Myr; Allers et al. (2006); Luhman & Rieke (1999); Prato et al. (2003)) were extracted
from the literature (Kraus et al. 2011; Kraus & Hillenbrand 2009b; Duchêne et al. 2007;
Ratzka et al. 2005; Haisch et al. 2004, 2002; White & Ghez 2001; Köhler & Leinert 1998;
Reipurth & Zinnecker 1993; Leinert et al. 1993) (see also Table 1 for references on each
object).

The companionship and membership to Taurus or Ophiuchus in our sample were examined using the literature because the sample may include suspicious secondary stars not physically associated to the primary, or older systems than 1–2 Myr. In Taurus, coevality ($d\Delta \log(t)$) between primary and secondary stars has been indicated to be <0.4 dex which is significantly smaller than 0.58 dex estimated from the random paring of single stars (Kraus & Hillenbrand 2009a). In our initial 33 binaries, the systems whose ages are known and coevality is larger than 0.4 dex are 2MASS J04554757+3028077, HP Tau/G2, and DK Tau.

The age difference of $d\Delta \log(t) \sim 0.8$ was found for DK Tau between the primary and the secondary stars, but a possible systematic error was implied in this age estimation (Kraus & Hillenbrand 2009a). In addition, in order to explain the estimated size for the circumprimary disk, the presence of a companion is favored right at the distance of the secondary candidate. Therefore, we retained DK Tau in our binary sample while excluded 2MASS J04554757+3028077 and HP Tau/G2. In addition, RXJ 0437.4+1851, NTTS 040142+2150, and V1117 Tau systems are speculated to be older compared to the typical ages of Taurus based on the Li test, or to be unassociated to the Taurus region judging from the proper motions (Sestito et al. 2008; Wichmann et al. 2000). Since contamination of these sources can affect the discussion of disk frequency at the age of 1–2 Myr, we eliminated these sources from our sample. For Ophiuchus, VSSG 23 was removed from our sample due to their non-coevality ($d\Delta \log(t) \sim 1$; Prato et al. (2003)). Unfortunately, sufficient data on coevality and proper motions were not available for many of the Ophiuchus sources, and these systems remain to be included in the sample as binary candidates. As a result, six systems were eliminated from the initial 33 binaries, and 27 systems were analyzed in this paper.

It should be noted that our sample includes triple and quadruple systems consisting of the close binaries with separations of $\sim 0\!''\!01$–$0\!''\!1$ and the other widely separated components; 2E 1628.2-2423 (Mathieu et al. 1989), V1001 Tau (White & Ghez 2001), RXJ 0435.9+2352 (Köhler & Leinert 1998), L1689 SNO2 (Ratzka et al. 2005), and

2MASS J04251767+2617504 (Duchêne 1999). Because the close components should exhibit rapid disk clearing (Monin et al. (2007); Cieza et al. (2009); Kraus et al. (2012)), whether this parameter affects our discussion will be explored in later sections. Binarity in these systems, especially those that are widely separated, has yet to be confirmed by multi-epoch astrometry; therefore, many of these systems are candidates of binaries. Table 1 summarizes the projected separations and spectral-types taken from literature for our sampled systems.

Since the closely spaced systems cannot be analyzed by aperture photometry, they were divided into individual components by profile fitting to the *Spitzer*/IRAC archival images, as described in the following section. Fortunately, many of the binaries are located in regions surveyed in the "From Molecular Cores to Planet-Forming Disks" (c2d) legacy project (Evans et al. 2003). The IRAC data were acquired from the NASA/IPAC Infrared Science Archives[1]. Following basic calibration, cosmic rays were removed by mosaicking the post-BCD data (IRAC Instrument Handbook[2]), and photometry was performed on the mosaicked post-BCD images. The pixel scale of the post-BCD images was $0\rlap{.}''6$, two times as small as the native pixel size. The data were obtained over two effective integration times: `long` (10.4 sec) and `short` (0.4 sec). Photometry was generally carried out using the `short`-exposure frames, because these frames yield better fits to the stellar profile. The exceptions were the faint ($\lesssim 9$ mag) binaries for which the `long`-exposure images were used.

---

[1]http://irsa.ipac.caltech.edu/data/SPITZER/docs/spitzerdataarchives
[2]http://irsa.ipac.caltech.edu/data/SPITZER/docs/irac/iracinstrumenthandbook/

2.2 PSF Fitting Photometry

2.2.1 Photometry for Sources Having Nearby Single Stars

The images of the primary and secondary stars overlapped at binary projected separations of $\sim 2''$–$4''$. Therefore, we resolved the primary and secondary stars by χ^2 fitting using a stellar profile model, which determined six variables; the positions of the primary and secondary star (x and y for each star) and the scaling factors of the profile models. The six simultaneous equations were solved by the Newton–Raphson method. The initial position of the primary star was set at the location of the brightest pixel and was adjusted to minimize χ^2. The location of the secondary star was assumed to match its relative position to the primary star, reported in the literature. The location of the secondary star was then adjusted to minimize χ^2. The initial scaling factor for the profile model was determined to match the pixel intensity to its observed intensity at the initial stellar position. To create the profile model, the images of five single stars near the binary system were averaged using the PSF task in IRAF[3]. The uncertainty on the observed PSF used for the χ^2 fitting was estimated as follows. First, each of the five single stars was fitted with the same fitting tool and profile model, and the standard deviation σ stored in the 2D uncertainty image in the post-BCD dataset (*_unc.fits) as a weight. Here, the σ contained dark noise, flat-fielding error, read-out noise, and Poisson noise. At each pixel, the difference between the observed value and the fitted model profile reached ~ 10–20%, exceeding those predicted from the uncertainty image by a few orders of magnitude. Thus, to further consider the possible uncertainty associated with the observed PSF, the mean of the residuals between the observed profile and the model was calculated over the five stars, then applied to the χ^2 fitting as a new σ. Averaged stellar profile model, together with its σ, yielded plausible results ($\chi^2/\mathrm{d.o.f.} \sim 1$). We also confirmed the quality of the fitting in the residual image and that the location of each star was consistent in the

---

[3]IRAF is distributed by the National Optical Astronomy Observatories, which are operated by the Association of Universities for Research in Astronomy, Inc., under cooperative agreement with the National Science Foundation.

different wavebands, even for closely spaced systems ($\sim 2''$–$3''$). The χ^2 of all targets are summarized in Table 1. The widely separated systems ($\gtrsim 4''$) were fitted with the same tool to prevent systematic error introduced by the fitting tool.

2.2.2 PSF-Fitting for Sources Lacking Nearby Single Stars

The averaged stellar profile was unable to be obtained for one system (TYC 1289-513-1), because no nearby single stars were found in the same field. This system was fitted by the template point response function (PRF) provided by the IRAC team. Since the FWHM of the template function was always smaller than that of the observed PSF, it was convolved with a Gaussian function. The values store in the post-BCD uncertainty image was used as σ for the χ^2 fitting. The resulting $\chi^2/\mathrm{d.o.f.}(\gtrsim 1000)$ were unacceptably large, which should be plausible because the uncertainty associated with the observed PSF was ignored. We verified the effect of variation in the stellar profile on the photometric results using systems that permitted an averaged stellar profile. The measured magnitudes between the Gaussian-convolved template and averaged stellar profile fitted to the data differed by $\lesssim 0.1$ mag in all IRAC wavebands. Therefore, we concluded that the σ in the uncertainty files were excessively small and responsible for the huge χ^2, but the Gaussian-convolved template was reasonably fitted to the data. In Figure 2.1, as a reference, we show the (a) IRAC image data of the binary sample, IT Tau, with a separation of 2", (b) Gaussian-convolved template, and (c) residual image.

2.2.3 Photometric Error

The photometric error can be estimated using the revised σ obtained from the empirical PSF constructed from the stellar profiles of five nearby single stars. The best-fitted scaling factor of the profile was varied until the reduced-χ^2 changed by 1.17 (d.o.f. $= 6$), and the flux difference created by this process was considered as the error in the measured magnitude. The uncertainty estimates of several binaries were consistent within 10% in all

(a) Image of IT Tau for every IRAC bands   (b) Gaussian-convolved template   (c) Residual image
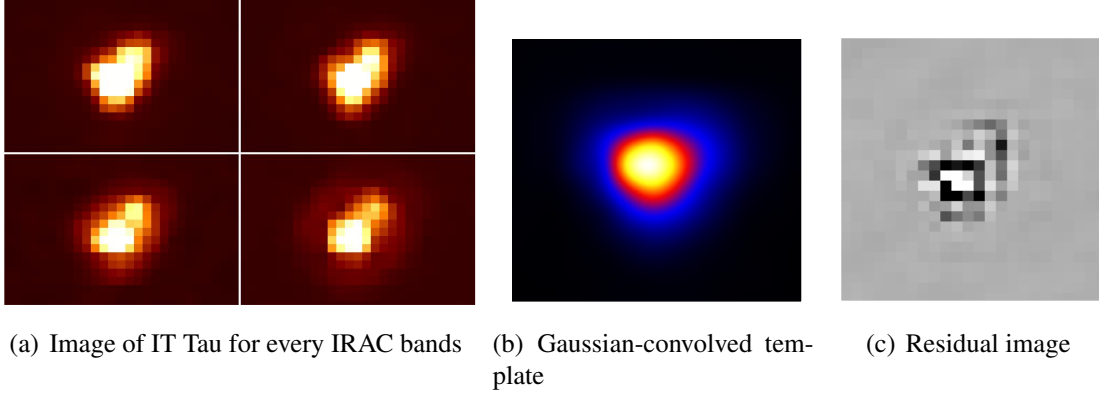
Figure 2.1: (a) Image of IT Tau at four wavelengths. Top left is ch1, top right is ch2, left lower is ch3, and right lower is ch4. 3.6, 4.5, 5.8, and 8.0 μm are shown in top left, top right, bottom left, and bottom right, respectively. (b) Gaussian-convolved template for 3.6 μm. (c) Residual image after profile fitting using (b) image is shown.

four wavebands. Comparing the measured magnitudes with those obtained by Gaussian-convolved template fitting, we estimated a conservative photometric error of 0.14 mag in all IRAC bands.

2.2.4 Sources Lacking Photometric Data in Some IRAC Bands

Photometry in some IRAC bands was precluded in three systems, because the primary and secondary stars were obscured by the large brightness contrast (at 3.6 μm for DoAr 24E and at 4.5 and 5.8 μm for HN Tau B) and by the overlap between the secondary position and the latent image caused by an exceptionally bright primary star (at 8.0 μm for 2E 1628.2-2423). The measured magnitudes of all targets are summarized in Table 1.

Table 2.1: Characteristics of Sampled Binary Systems: Taurus – For individual binary systems, spectral type (Column 3) and measured IRAC magnitudes (Columns 4–7) of the primary and secondary members are shown in the first and second row, respectively. The second column lists the projected separations of the systems. The eighth column lists the χ^2/d.o.f. given by the profile fitting at each IRAC wavelength. References are given in parentheses in Columns 2–3 (see below). The typical photometric error in the PSF fitting photometry is 0.14 mag.
[†] Denotes a candidate of a triple or quadruple system.
[*] Denote a mixed system.
(1) White & Hillenbrand (2004); (2) White & Ghez (2001); (3) Kraus et al. (2011); (4) Correia et al. (2006); (5) Prato et al. (2003); (6) Kraus & Hillenbrand (2009b);(7) Wilking et al. (2005); (8) Kraus & Hillenbrand (2009a); (9) Monin et al. (1998); (10) Connelley & Greene (2010); (11) Kraus & Hillenbrand (2007); (12) Duchêne et al. (2007); (13) Köhler & Leinert (1998); (14) Reipurth & Zinnecker (1993); (15) Ratzka et al. (2005); (16) Haisch et al. (2004); (17) Haisch et al. (2002); (18) Greene & Meyer (1995); (19) Luhman & Rieke (1999); (20) Walter et al. (1994); (21) Kenyon & Hartmann (1995); (22) Duchêne et al. (1999).

Systems	Separation ($''$)	SpT.	[3.6] (mag)	[4.5] (mag)	[5.8] (mag)	[8.0] (mag)	χ^2/d.o.f. (ch1–4)
		Taurus					
JH 223	2.07 (3)	M2 (11)	9.10	8.88	8.39	7.88	1.0, 0.4, 0.7, 1.0
		M6.5 (11)	11.26	11.06	10.63	9.85	
CoKu Tau 3	2.1 (14)	M1 (11)	7.51	6.98	6.51	5.67	0.8, 1.0, 1.5, 1.6
		M5 (11)	9.17	8.99	8.50	7.99	
DK Tau	2.3 (2)	K9 (9)	6.21	5.77	5.50	4.87	1.0, 1.2, 1.2, 1.3
		M1 (9)	7.84	7.47	7.26	6.72	
CIDA 9	2.34 (3)	M0 (11)	9.33	8.74	8.09	7.08	1.6, 1.0, 0.9, 1.3
		M2.5 (11)	11.49	11.01	10.70	9.82	
HK Tau	2.34 (3)	M1 (1)	7.81	7.49	7.14	6.62	0.7, 0.8, 0.4, 0.8
		M1 (1)	11.47	10.91	10.64	9.69	
IT Tau	2.39 (2)	K3 (22)	7.54	7.16	6.82	6.32	1.8, 1.9, 0.8, 0.7
		M4 (22)	9.05	8.68	8.11	7.51	
V1001 Tau[†]	2.62 (2)	K8 (9)	6.69	6.27	5.88	5.33	0.8, 1.8, 1.1, 0.9
		M0 (9)	7.90	7.38	7.11	6.06	
HN Tau	3.10 (6)	K5 (4)	7.00	6.34	5.65	4.76	1.3, 3.0,—,—
		M4.5 (22)	11.11	10.51	—	—	
V710 Tau[*]	3.17 (2)	M1 (21)	7.99	7.80	7.19	6.57	1.6, 4.1, 1.4, 3.1
		M3 (21)	8.39	8.45	8.26	8.29	
2MASS J04251767+2617504[†]	3.4 (2)	K7 (13)	8.44	8.38	8.34	8.31	2.9, 1.2, 1.8, 1.3
		M3 (13)	9.10	9.05	8.98	9.00	
BBM92 14	4.06 (12)	M2 (10)	6.55	5.84	5.32	4.57	1.2, 1.2, 1.6, 2.2
		M2 (10)	7.13	6.53	5.97	5.14	
TYC 1289-513-1	6.87 (13)	—	8.68	8.67	8.57	8.47	—
		—	10.69	10.69	10.58	10.47	
RXJ0435.9+2352[†]	11.3 (13)	—	8.79	8.78	8.76	8.63	9.2, 5.3, 2.3, 0.8
		—	10.82	10.98	10.84	10.69	
GI Tau	13.14 (6)	K6 (21)	6.43	6.14	5.90	4.90	0.8, 1.0, 1.8, 1.0
		M0 (21)	6.83	6.38	5.81	4.82	
FZ Tau	17.17 (6)	M0 (4)	6.28	5.75	5.28	4.62	1.5, 0.7, 1.6, 1.7
		K7 (21)	7.19	6.86	6.53	6.07	

Table 2.2: Characteristics of Sampled Binary Systems: Ophiuchus

Systems	Separation (")	SpT.	[3.6] (mag)	[4.5] (mag)	[5.8] (mag)	[8.0] (mag)	χ^2/d.o.f. (ch1–4)
		Ophiuchus					
DoAr 24 E	2.07 (15)	G6 (7)	—	5.03	4.62	3.88	—,1.8, 2.1, 1.4
		K4.5 (7)	—	6.25	5.77	4.93	
L1689 SNO2[†]	3.01 (15)	M2 (10)	6.34	5.50	4.76	3.96	—
		M2 (10)	8.04	7.72	7.37	6.76	
WSB71a	3.56 (15)	K2 (5)	6.62	6.08	5.46	4.75	1.7, 0.7, 2.4, 1.3
		M6 (5)	9.49	9.15	8.53	7.80	
ROXRF 36	3.59 (15)	—	9.26	9.16	8.13	9.01	1.2, 0.8,—, 0.2
		—	10.09	9.96	9.80	9.77	
WL 18	3.62 (15)	—	8.67	8.00	7.84	7.35	2.0, 2.7, 1.5, 0.3
		—	11.06	10.68	10.34	10.22	
2MASS J16264848-2428389	4.15 (16)	—	9.08	8.21	7.56	6.74	1.9, 3.3, 1.4, 1.2
		—	10.38	9.71	8.94	8.25	
2E 1628.2-2423[†*]	4.3 (14)	G0 (20)	6.37	5.96	5.30	—	2.0, 1.0, 2.7,—
		K5 (20)	7.68	7.59	7.50	—	
2MASS J16262097-2408518[*]	5.21 (15)	M3 (4)	9.14	9.13	9.06	8.98	2.2, 1.0, 0.4, 0.2
		M7 (4)	10.89	10.53	10.10	9.37	
2MASS J16271757-2428562	8.55 (16)	F7 (18)	7.82	6.95	6.47	6.49	5.2, 7.8, 6.0, 2.0
		M4 (19)	8.36	7.35	6.51	5.95	
2MASS J16263682-2415518	9.08 (12)	M0 (3)	8.17	7.85	6.29	5.27	4.1, 2.3, 2.7, 1.5
		M5 (7)	10.25	10.23	9.74	9.14	
UCAC2 21797671[*]	10.3 (14)	M2 (7)	8.83	8.48	8.23	7.72	0.8, 1.9, 1.7, 0.8
		M4.5 (7)	10.07	10.04	9.96	9.87	
2MASS J16262404-2424480	10.47 (17)	—	6.43	4.83	4.18	3.44	1.6, 5.0, 2.9, 3.8
		—	7.44	6.55	5.78	5.04	

2.3 Result

2.3.1 Infrared Excess at 8.0 μm

We first examined whether the emission of the individual components in the binary systems exceeds the photospheric level at 8.0 μm. Figure 2.2 shows a histogram of the color $[3.6] - [8.0]$ distribution of the sources for which the photometry at 3.6 and 8.0 μm is available. The clear gap in the figure, occurring at $[3.6] - [8.0] \sim 0.6$, is considered to divide the sources with and without excess at 8.0 μm. The excess frequency (defined as excess sources/(excess sources+non-excess sources), and hereafter denoted EF) of the primary and secondary stars were $79^{+5}_{-7}\%$(19/24) and $73^{+6}_{-7}\%$(16/22), respectively.

Figure 3.2 shows color-color diagrams of $[3.6] - [4.5]$ (*left*) and $[3.6] - [5.8]$ (*right*) against $[3.6] - [8.0]$. The objects with $[3.6] - [8.0] \lesssim 0.6$ are gathering near the origins of the diagrams, indicating that they are also photospheric at 4.5 and 5.8 μm. In contrast, the sources with $[3.6] - [4.5] \gtrsim 0.2$ and $[3.6] - [5.8] \gtrsim 0.4$, located in the correlation extending to the upper right of the diagrams, are tend to have excess emission at 8.0 μm ($[3.6] - [8.0] > 0.6$) in addition to 4.5 and 5.8 μm. However, it should be noted that identification of the excess sources at 4.5 μm is difficult because no clear color break occurs. Although we can see a clear gap at $[3.6] - [5.8]$ colors around 0.4, some excess sources overlap with the non-excess sources when considering the typical uncertainty of the $[3.6] - [5.8]$ colors.

The 8.0 μm excess was detected relative to 3.6 μm, rather than absolutely, based on the color $[3.6] - [8.0]$. In addition, the excess at 4.5 and 5.8 μm is sometimes difficult to be identified from the color-color diagrams. Therefore, we additionally checked the presence of excess emission using the spectral energy distributions (SEDs). Fitting a stellar photosphere requires photometry in one or more optical bands in addition to J band. The photometric values in the optical bands (B, V, R, I) were taken from the USNO-B1 Catalog (Monet et al. 2003). For the sources for which the resolved photometric values were

unavailable from the catalog, we used the resolved data in optical bands from additional references (Zacharias et al. 2005; Torres et al. 2006; Grankin et al. 2007; Herbig & Bell 1988). The J-band magnitudes were taken from the 2MASS All-Sky Catalog of Point Sources (Cutri et al. 2003). If these magnitudes were unavailable from the catalog, the resolved data in the J band were extracted again from additional references (Kraus & Hillenbrand 2007; Connelley & Greene 2010; Moneti & Zinnecker 1991; Chavarría K et al. 2000). The spectral types were available for many of our sample sources from previous studies (see Table 1). Free parameters for the fitting are A_V and the scaling factor of the photosphere, corresponding to the radius of the star and distance to the star-forming regions. To model the stellar photosphere at high and low effective temperature, we adopted the models of Krucz (Kurucz 1993) and AMES-Cond (Allard et al. 2001), respectively. For sources with known A_V but unknown optical-band magnitudes, the quoted A_V values were used to correct for extinction in the SEDs (Furlan et al. 2011; Chavarría K et al. 2000; Wahhaj et al. 2010; Evans et al. 2009; Currie & Sicilia-Aguilar 2011; McClure et al. 2010; Bontemps et al. 2001). The data required for the SED fitting were unavailable for 12 of the sources, and we do not discuss them below.

The excess at 8.0 μm was estimated based on the SEDs for 37 sources with the available photometry at this wavelength. All the sources which appear at $[3.6] - [8.0] > 0.6$ show the excess at 8.0 μm in their SEDs, while none of them at $[3.6] - [8.0] < 0.6$ exhibit an excess emission. We also confirmed that 34 out of the 37 sources ($92^{+4}_{-6}\%$) showed or did not show excess at both 3.6 and 8.0 μm. Six sources (ROXRF 36 A and B, TYC 1289-513-1 A and B, RXJ0435.9+2352 A and B) were excluded in the above calculation, because they lacked spectral-type data. However, these sources were assumed non-excess sources in all IRAC bands, since they were classified as Class III based on $K - [8.0]$ data (see Section 2.3.3). If the six sources are included, 40 out of the 43 selected sources ($93^{+3}_{-6}\%$) either show or do not show excess at both 3.6 and 8.0 μm.
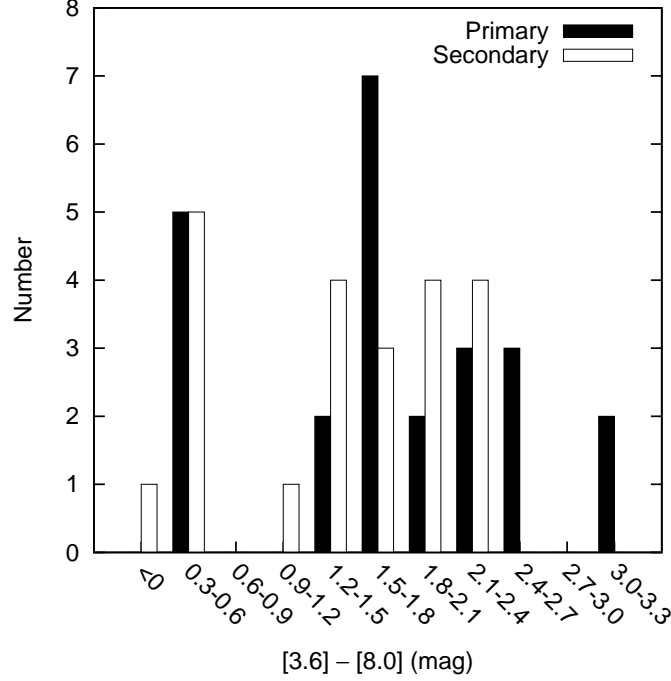
Figure 2.2: Histogram of the color of $3.6 - 8.0$ shown by primary (*filled*) and secondary (*hollow*) sources. Class I sources (see Section 4.2) are not included in this plot.

2.3.2 Excess at Other IRAC Wavelengths

The occurrence of excess emission and the relation with the 8.0 μm excess were also examined at 4.5 μm and 5.8 μm in the SEDs. Thirty nine out of 54 sources were used since the photometric data were obtained for them at these wavelengths and 8.0 μm. Note that the sample for 5.8 μm is different from that of 4.5 μm, although the sample size is the same. At 4.5 μm, 37 out of the 39 sources ($95^{+3}_{-5}\%$) showed excess or non-excess at both wavelengths (4.5 μm and 8.0 μm), and at 5.8 μm, 38/39 sources ($98^{+2}_{-4}\%$) present the same characteristics. These results indicate that the presence or non-presence of excess emission at 8.0 μm behaves similarly at 3.6, 4.5, and 5.8 μm. The exceptions are three sources that show excess at 8.0 μm but not at the shorter wavebands. 2MASS J16263682-2415518 B, V 710 Tau A, and JH 223 A begin to exhibit significant excess from 8.0, 5.8, and 4.5 μm, respectively. These three sources are further discussed in the appendix.
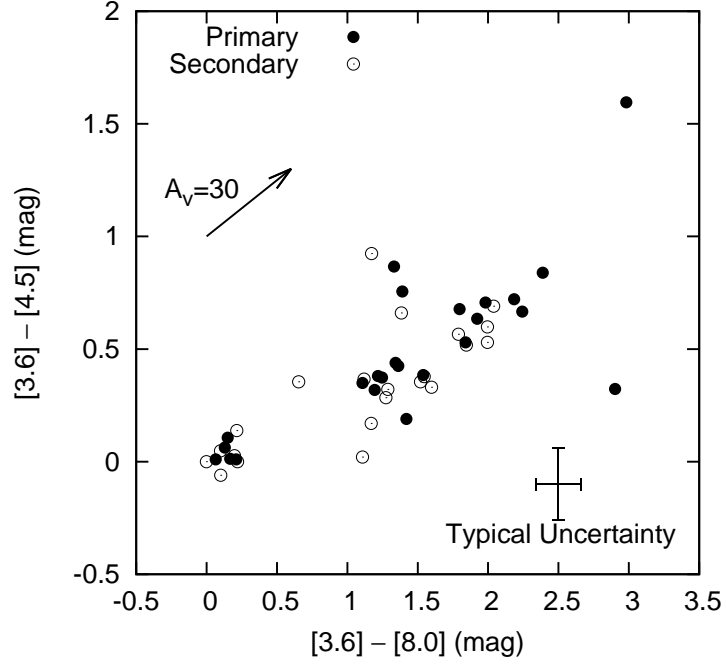
(a) Color-color diagrams of [3.6]−[4.5]
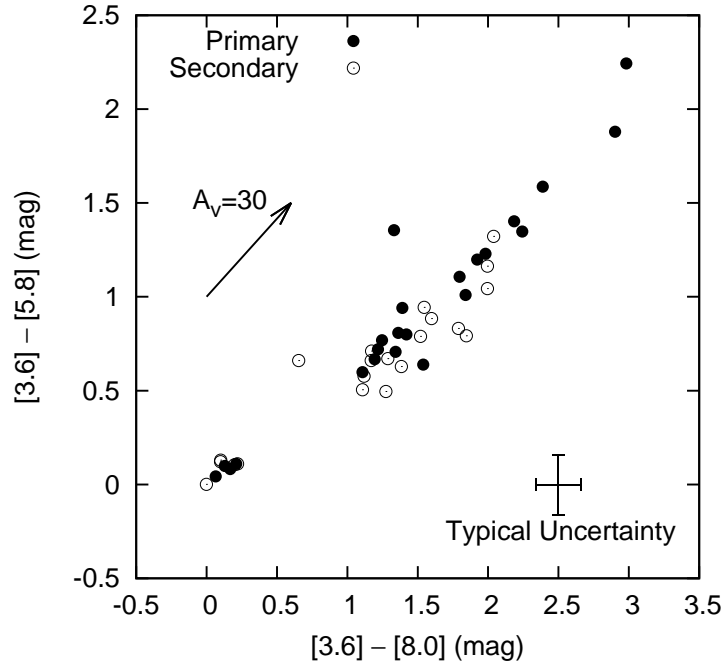
(b) Color-color diagrams of [3.6]−[5.8]

Figure 2.3: Color-color diagrams of $[3.6] - [4.5]$ (Figure a) and $[3.6] - [5.8]$ (Figure b) against $[3.6] - [8.0]$. *Filled circles* show primary stars and *hollow circles* indicate secondary stars. The extinction vector in the IRAC bands is based on the simple-fit formula reported by Indebetouw et al. (2005). Class I sources (see Section 4.2) are not included in this plot.

2.3.3 $[3.6] - [8.0]$ **Colors for Sources Lacking Photometric Data at 8.0 μm**

Following the results in the previous subsection, we evaluate the existence of a circumstellar disk through the color of $[3.6] - [8.0]$ since it shows the most distinct boundary between excess and non-excess stars. However, the magnitudes at 8.0 μm were unavailable for two sources (2E 1628.2-2423 and HN Tau B), thus we attempted to speculate whether the sources lacking photometric data at 8.0 μm had excess at this wavelength (i.e., $[3.6] - [8.0] > 0.6$). 2E 1628.2-2423 A shows significant excess at 3.6–5.8 μm, as confirmed from the SED, thus it is plausible to categorize it as an 8.0 μm excess source. On the contrary, 2E 1628.2-2423 B exhibited no excess at 3.6–5.8 μm. Considering the rarity of sources that first show excess at 8 μm ($\sim$6%), this object was presumed as a non-excess source at 8.0 μm. The value of $[3.6] - [4.5] = 0.41$ for HN Tau B (M4.5; Kraus & Hillenbrand (2009a)) is significantly higher than the photospheric color of an M5-type star (-0.08; Luhman et al. (2010)). Therefore, this source most likely has 8.0 μm excess. Note that the recent ALMA observations failed to detect the secondary source in dust continuum at 850 μm and 1.3 mm (Akeson & Jensen 2014), but the secondary indicated the Hα emission and was classified as a classical T Tauri star (e.g., Duchêne (1999)).

Photometry at 3.6 μm was not obtained for both components in DoAr 24 E (see Section 2.2), and hence the $[3.6] - [8.0]$ colors were unavailable. However, they generated the significant excess at 4.5–8.0 μm, as confirmed from the SEDs. Therefore, they can be categorized as excess sources. In summary, in the statistical discussion in later sections, we regard 2E 1628.2-2423 A, HN Tau B, and DoAr 24 E as excess sources and 2E 1628.2-2423 B as a non-excess star.

Our sample includes Class I sources that might still be surrounded by envelopes. To simplify the discussion and calculate the excess frequency for Class II and III sources only, we excluded the Class I sources as follows. Classes were identified from the $K - [8.0]$ color, adopting the criterion of Lada (1987). That is, sources satisfying $K - [8.0] >$

3.9 were regarded as Class I, $1.14 < K - [8.0] < 3.9$ as Class II, and $-0.26 < K - [8.0] <$ 1.14 as Class III. The JHK-bands magnitudes were taken from the 2MASS Catalog or additional references (Kraus & Hillenbrand (2007); Connelley & Greene (2010); Moneti & Zinnecker (1991); Chavarría K et al. (2000)). For the sources lacking the SED fitting (Section 2.3.1), the A_V values for the color correlation were taken from previous studies (Furlan et al. (2011); Kraus & Hillenbrand (2009a); Wahhaj et al. (2010); Chavarría K et al. (2000); Evans et al. (2009); McClure et al. (2010); Currie & Sicilia-Aguilar (2011); Bontemps et al. (2001)). As a result, 35 out of the 54 sources with both $K - [8.0]$ and A_V data available were divided into their respective classes, of which two sources (2MASS J16271757-2428562 B and CIDA 9 A) were identified as Class I. The remaining 19 sources lacking $K - [8.0]$ or A_V data were classified based on the $J - H \ versus \ H - K$ color-color diagram. In this classification, we employed the JHK colors of unreddened main sequence of Koornneef (1983) (Lada & Adams 1992) and the locus of T Tauri stars derived by Meyer & Hillenbrand (1997). In addition, we assumed the interstellar reddening raw estimated by Koornneef (1983), Bessell & Brett (1988), and Martin & Whittet (1990). As a result, one source (2MASS J16262404-2424480 B) was classified as Class I. The 51 sources or 24 systems not classified as Class I were used in the analyses in Section 5.

2.4 EFFECT OF BINARITY FOR IRAC EXCESS AND DIFFERENCES FROM SINGLE STARS

In this section, we show whether primary and secondary stars share the same behavior regarding the presence of IRAC excess. In addition, we discuss the dependence of EF on binary separation and the difference of the EF between the binary systems and single stars.

2.4.1 Mixed Systems

In Figure 2.4, the $[3.6] - [8.0]$ color of the secondary star is plotted against that of the primary star. As described in the previous sections, the clear color break at ~ 0.6 divides the sources showing excess from those not showing excess. Twenty systems out of the 24 binaries ($83^{+8}_{-11}\%$) show excess or non-excess associated with both components. The remainder ($17^{+11}_{-8}\%$) show excess emission from only one of the binary components ("mixed" binaries). The number of systems showing excess solely from the primary and secondary source is three ($13^{+9}_{-6}\%$) and one ($4^{+7}_{-4}\%$), respectively. To compare this mixed system ratio with the distribution of random sampling from a single star population, the EF of single stars was set to 70% (see Section 2.4.3). The probability of obtaining the observed number of mixed systems is $C^4_{24}(0.42)^4(0.58)^{20} \simeq 6 \times 10^{-3}$. This significantly low probability implies that the disappearance of excess emission from circumprimary and circumsecondary disks is strongly correlated. On the other hand, binomial statistical analysis revealed no preference for either component to exhibit excess; i.e., there is no significant difference between the ratio of systems showing excess solely from the primary source (3/4; $75^{+20}_{-36}\%$) and from the secondary source (1/4; $25^{+36}_{-20}\%$). The errors stated here represent the 1σ confidence interval containing the central 68% of the binomial distribution.

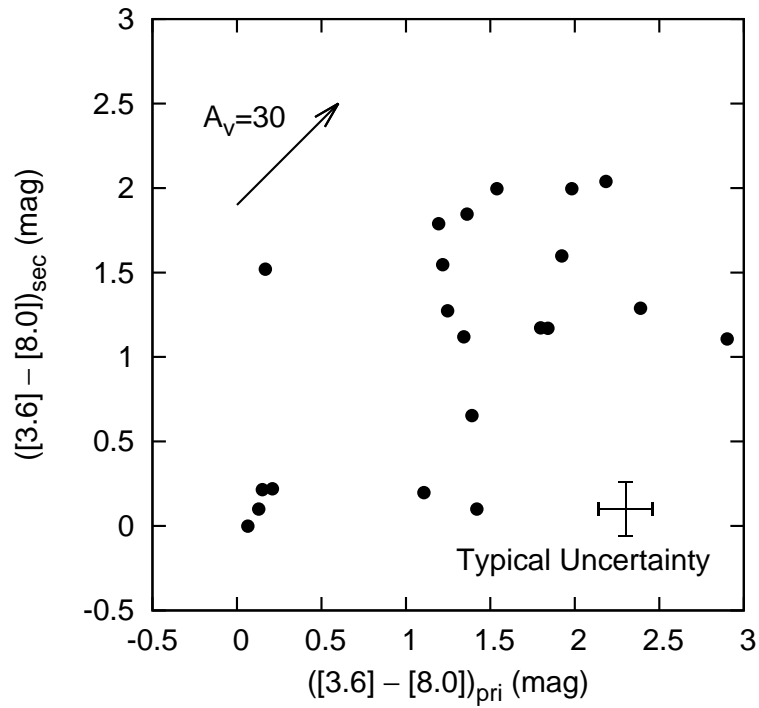Our sample includes five triple or quadruple systems with close ($\lesssim 0''.1 \simeq 15$ AU)

Figure 2.4: $[3.6] - [8.0]$ color of secondary *versus* primary stars. The extinction vector in the IRAC bands is based on the simple-fit formula reported by Indebetouw et al. (2005). The typical error in the measured color is 0.20 mag. The sources without measurements of $[3.6] - [8.0]$ for both binary components are not included in the figure.

binaries corresponding to the primary or secondary component. Binaries with separations closer than $\sim$40 AU show a lower frequency of infrared excess compared with single or wide binary sources (e.g., Monin et al. (2007); Cieza et al. (2009); Kraus et al. (2012)). This suggests that these triples and quadruples should have a higher fraction of mixed pairs. However, the EF does not significantly change when these five systems are excluded from the analysis. In this case, in 16 out of 19 systems ($84^{+8}_{-13}\%$), both members either show or do not show excess emission. The number of mixed systems is 3 ($16^{+13}_{-8}\%$ of the sample), and the conclusion is unaltered.

The four mixed systems are V710 Tau, 2MASS J16262097-2408518, 2E 1628.2-2423, and UCAC2 217971. They can be in the evolutionary transition between disk-bearing and disk-less binaries. Based on the observed ratio of mixed systems and the ages of Taurus and Ophiuchus which are $\sim$$10^6$ yrs, the duration of the mixed phase can be speculated as $\lesssim$$10^5$ yrs. Alternatively, as mentioned above, it is known that the existence of a tight companion leads to a shorter timescale for disk clearing. Since very high angular-resolution observations have not been reported for the 4 binaries, we cannot exclude the possibility of these systems possessing undetected close ($\lesssim$10 AU) companions.

The rarity of mixed systems contradicts the concept of random pairing suggested in previous studies. In their study of circumstellar disks in the Taurus region, White & Ghez (2001) reported that the disks at the separations wider than 210 AU are consistent with random pairing. This conclusion was inferred from the spatially resolved $K - L$ color and Hα data. More recently, Daemgen et al. (2012) suggested that random pairing occurs in the systems separated by more than 200 AU in the Orion Nebula Cluster. In contrast, our analysis indicates the correlation of primary and secondary components in the separation range of $\simeq$280–2400 AU. Different sample size may account for the disagreement since our sample of 24 systems is approximately three times greater than those of the previous works. Another potential source of disagreement is the disk indicators. In the above-mentioned studies, gas accretion and dust emission were probed from the inner-most regions. By contrast, the $[3.6] - [8.0]$ color traces dust emission from the farther,

~ 1 AU region of the disk.

2.4.2 Dependency of EF on Separation

The $[3.6] - [8.0]$ color is plotted as a function of binary projected separation (a_p) in Figure 2.5. The horizontal axis is converted from arc seconds to AU, assuming that each star-forming region is located at 140 pc. In this figure, more closely separated binary companions ($a_\mathrm{p} \simeq 280$–450 AU) tend to show excess emission. We verified the dependence of the EF on binary separation and distinguished the regions exhibiting high and low EFs employing Fisher's exact test below.

To identify the different EF regions, we split our sample into two groups based on whether the projected separation was larger or smaller than the separation a_c and assessed whether EF differed between the groups. Figure 2.6 shows the results of Fisher's test applied to the three sub-populations; primary, secondary, and both components. The *left* (a) and *right* (b) panels show Fisher's p-value and EF, respectively, as a functions of a_c. In the *left* (a) panel, the p-value initially decreases at smaller a_c, and is minimized at $a_\mathrm{c} \simeq 450$ AU. This is because the sample size with $a_\mathrm{p} < a_\mathrm{c}$ increases while maintaining the high EF, whereas that of binaries with $a_\mathrm{p} > a_\mathrm{c}$ remains at $\sim 75\%$ as shown in the *right* (b) panel. Fisher's exact test clarified that the EFs of more closely and widely separated systems are different with a boundary at $\simeq 450$ AU, at the significance of 1–2σ for each binary component. Including both primary and secondary sources in the analysis, Fisher's test gave the significance of 2–3σ. It is notable that the EF is very high ($\sim 100\%$) at $a_\mathrm{p} \lesssim 450$ AU for each primary and secondary subpopulation, and naturally for the sample including both components (*right* (b) panel of Figure 2.6).

2.4.3 Comparison with Single Stars

To compare the EFs between the binary systems with $a_\mathrm{p} \lesssim 450$ AU and single stars, we first estimated the EF of single stars ($\mathrm{EF_{single}}$) in Taurus and Ophiuchus. In Taurus, the
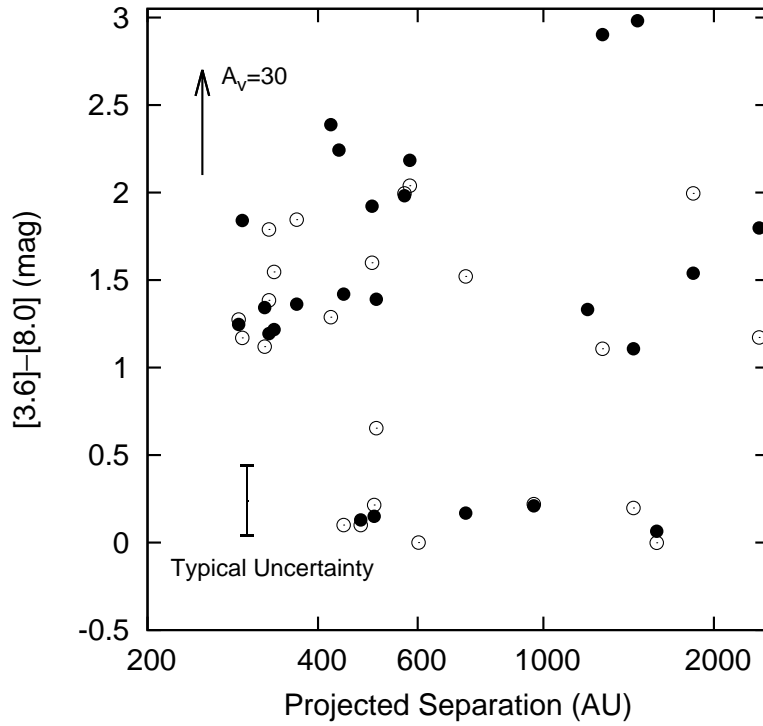
Figure 2.5: $[3.6] - [8.0]$ *versus* binary separation for primary (*black circles*) and secondary (*unfilled circles*) stars. Separation was converted to physical distance (in AU) using the distance to each star-forming region (140 pc). Note that the separation is the projected separation. The sources of excess emission are clustered around 280–450 AU. The sources without measurements of $[3.6] - [8.0]$ are not included in the figure.
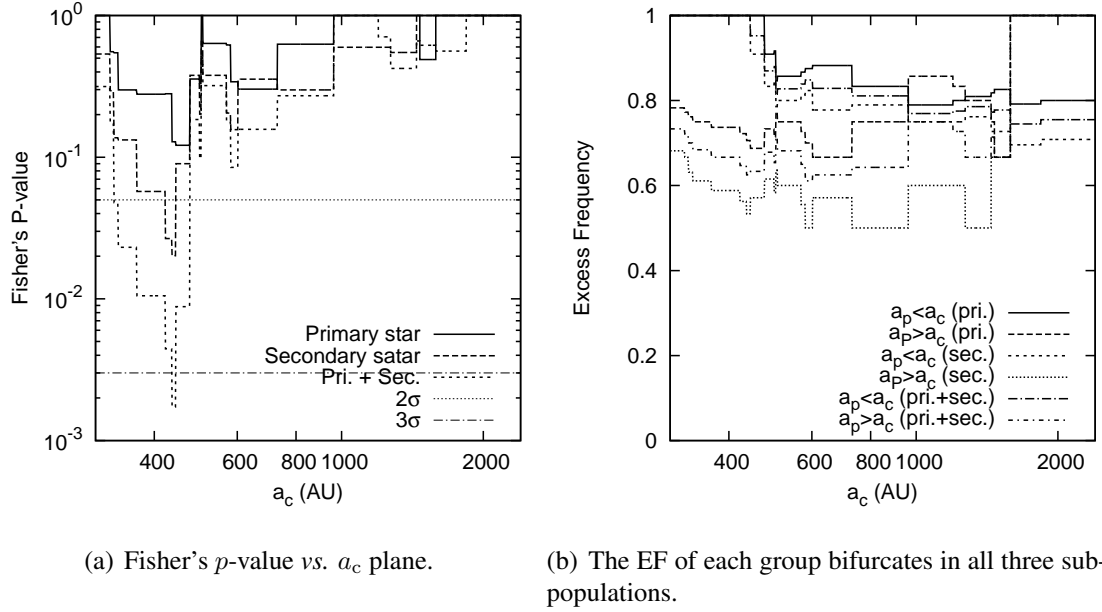
(a) Fisher's p-value *vs.* a_c plane.

(b) The EF of each group bifurcates in all three sub-populations.

Figure 2.6: This figure shows the significance of EF differences between *closer* ($a_p < a_c$) and *wider* ($a_p > a_c$) binary systems. (a): Fisher's p-value *vs.* a_c plane. The differences in EF were tested by Fisher's exact test between two groups of the binary samples, divided by whether the projected separation exceeds a_c. The *solid*, *dashed*, and *dotted* line show the Fisher's p-value for primary, secondary, and primary+secondary sources, respectively. The *horizontal-dotted* and *dashed-dotted* line indicate the 2σ and 3σ levels, respectively. The minimum p-value occurs at ~450 AU. At this radius, the significance of the EF difference between $a_p < a_c$ and $a_p > a_c$ is maximized ($2\sigma < p < 3\sigma$ for each component and $>3\sigma$ for primary+secondary sources). (b): The EF of each group bifurcates in all three sub-populations.

sample of 39 stars was adopted from Kraus et al. (2012) because little contamination of tight binaries is expected given the unprecedented resolution ($\sim$ 15–20 mas; 2–3 AU) and sensitivity ($\Delta K \sim$ 5–6 at 40 mas;$\sim$ 7–15 M_J at $\sim$6 AU) in their observations.

The single stars in Ophiuchus were collected from Cieza et al. (2009). Unfortunately, the single nature of these stars is less clear compared to the Taurus stars and the sample can be contaminated by tight binaries. Since there is a possibility of EF lowered for single stars because of this contamination, we attempt to calibrate the EF for Ophiuchus stars based on the frequency of tight binaries found in Taurus, in the discussion later in this section.

The EF can be biased by stellar age. In fact, the disk frequency is well-correlated with the typical age of a star-forming region (Mamajek (2009)). Theoretically, the evolution of a pre-main sequence star at $\sim$1 Myr with a spectral type of G–M is characterized by a decrease in luminosity at a nearly constant temperature (Baraffe et al. (1998); Yi et al. (2001)). This means that an age can be substituted by stellar luminosity; that is, the higher the luminosity, the younger the star and *vice versa*. Thus, we checked whether the age dependence of $\mathrm{EF_{single}}$ existed in our sample through the luminosities, which were estimated from the SEDs. Sufficient data for the SED fitting were available for 31 Taurus and 62 Ophiuchus sources.

To examine the dependence of EF on luminosity, the Taurus sample was divided into two subpopulations of spectral types of G0–K7 and M0–M4, comprising 12 and 19 sources, respectively. Each subpopulation was then divided by luminosity into two groups of approximately the same size. The $\mathrm{EF_{single}}$ was determined from the $[3.6] - [8.0]$ colors. The magnitudes at these wavelengths were obtained from IPAC/Gator[4]. When the data were unavailable, the photometric results were extracted from literature (Wahhaj et al. 2010; Luhman et al. 2010). A systematic difference between the above-cited magnitudes and those measured with our PSF-fitting tool do not affect the EF comparison between single and binary systems, because in both cases, the $[3.6] - [8.0]$ distribution is clearly

---

[4]http://irsa.ipac.caltech.edu/applications/Gator/

separated into two groups of with and without the color excess. Using the same criteria ($[3.6]-[8.0] = 0.6$), the EFs of four subpopulations were indistinguishable (EF$\simeq$0.7–0.9), indicating that $\mathrm{EF}_\mathrm{single}$ does not significantly depend on luminosity. Thus, we infer that the $\mathrm{EF}_\mathrm{single}$ is independent of stellar age. Adding seven M0–M4 stars without sufficient observations for SED fitting, the 38 sources for Taurus gave the EF of 74% (28/38). The same analysis was applied to the Ophiuchus sample, and the similar result was obtained about the EF dependence on stellar luminosity. To equalize the comparison between the single and binary samples, we discarded one object of the spectral type later than M6 because our binary sample consists of <M6 members. The EF was calculated as 56% (34/61) for the Ophiuchus cample. The final sample of single stars consists of 38 in Taurus and 61 sources in the Ophiuchus regions.

The difference in EF between single and binary systems was investigated first using this whole sample of single stars. Out of 99 sources, 62 show excess ($[3.6] - [8.0] > 0.6$); i.e., $\mathrm{EF}_\mathrm{single}$ is 63% (62/99). This $\mathrm{EF}_\mathrm{single}$ was then compared with the EF of binaries with the separation of $a_\mathrm{p} < a_\mathrm{c}$, again using Fisher's exact test. Figure 2.7 shows the results for the three subpopulations (primary, secondary, and both). The *left* (a) and *right* (b) panels present the Fisher's p-value and EF, respectively, as functions of a_c. The most significant difference appears at $a_\mathrm{c} \simeq 450$ AU, because the EF of primary and secondary sources separated within $\sim$450 AU is unity as described in Section 2.4.2. This EF of each component is significantly ($>2\sigma$) higher than that of single stars of 63%. For the entire binary sample including *both* primary and secondary sources, Fisher's exact test gave the significance value of $>3\sigma$. This suggests that, if the companions are separated by $\sim$280–450 AU, dust emission occurs more frequently in binaries than in single stars.

However, since the 61 single stars in Ophiuchus have been less studied in high-angular-resolution compared to the stars in Taurus, the sample may include undetected close binaries. Considering a possible underestimate of $\mathrm{EF}_\mathrm{single}$, we attempted to calibrate $\mathrm{EF}_\mathrm{single}$ assuming the same fraction of close binaries (η_cb) and the rate of disk-bearing ones ($\eta_\mathrm{cb;disk}$) in Ophiuchus to that measured in Taurus. Kraus et al. (2012) found

(a) Fisher's p-value *vs.* a_c plane.

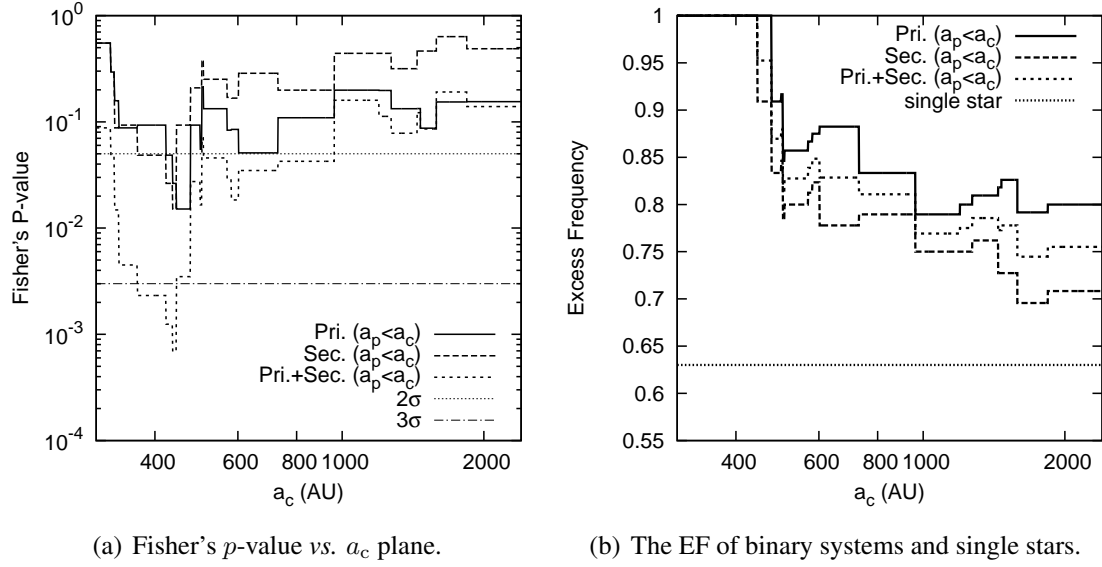(b) The EF of binary systems and single stars.

Figure 2.7: This figure shows the significance of EF differences between *closer binary systems* ($a_p < a_c$) and *single stars* without the calibration on possible tight companions described in the text. (a): Fisher's p-value *vs.* a_c plane for primary only, secondary only, and primary+secondary sources (*solid*, *dashed*, and *dotted* lines, respectively). The EF difference between the binary sample with $a_p < a_c$ and single stars was assessed by Fisher's exact test. The *horizontal-dotted* and *dashed-dotted* lines indicate the 2σ and 3σ levels, respectively. As in Fig. 2.6, the p-value is minimized at ~ 450 AU, where the difference in EF between binary systems with $a_p < a_c$ and single stars becomes most significant ($> 2\sigma$ for each component and $> 3\sigma$ for primary+secondary sources). (b): The EF of binary systems and single stars. The *horizontal-dotted* line indicates the $\mathrm{EF}_\mathrm{single}$ (63%).

that about 30% of their Taurus targets turned out to be binaries with 1–40 AU separations, and one third of the binaries showed the signatures of disks ($\eta_{\mathrm{cb}} = 0.3$, $\eta_{\mathrm{cb;disk}} = 1/3$) . Note that the presence of a disk was inferred through the excess emission in 2–8 μm in their study. If the EF of the single stars in Ophiuchus (hereafter $\mathrm{EF_{s;oph}}$) was determined with the same η_{cb} and $\eta_{\mathrm{cb;disk}}$, it yielded $\mathrm{EF_{s;oph}} = 0.659$. Thus, the number of single stars was estimated as 42 for Ophiuchus, in which 28 were considered to have excess emission. Combining the Taurus sample with the calibrated one for Ophiuchus, $\mathrm{EF_{single}}$ was found to be 70%. We conducted the Fisher's exact test using this sample. The Fisher's test demonstrated that the EF for each primary and secondary of the binaries is still significantly higher than that of single stars of 70% if the binary separation is $a_p \sim$280–450 AU ($\sim 2\sigma$; Figure 2.8). The significance of the difference is 2–3σ when estimated for the binary sample including both primary and secondary sources (see Figure 2.8). Therefore, we conclude the longer lifetime for binaries in this separation range.

(a) Fisher's *p*-value *vs.* a_c plane.   (b) The EF of binary systems and single stars.
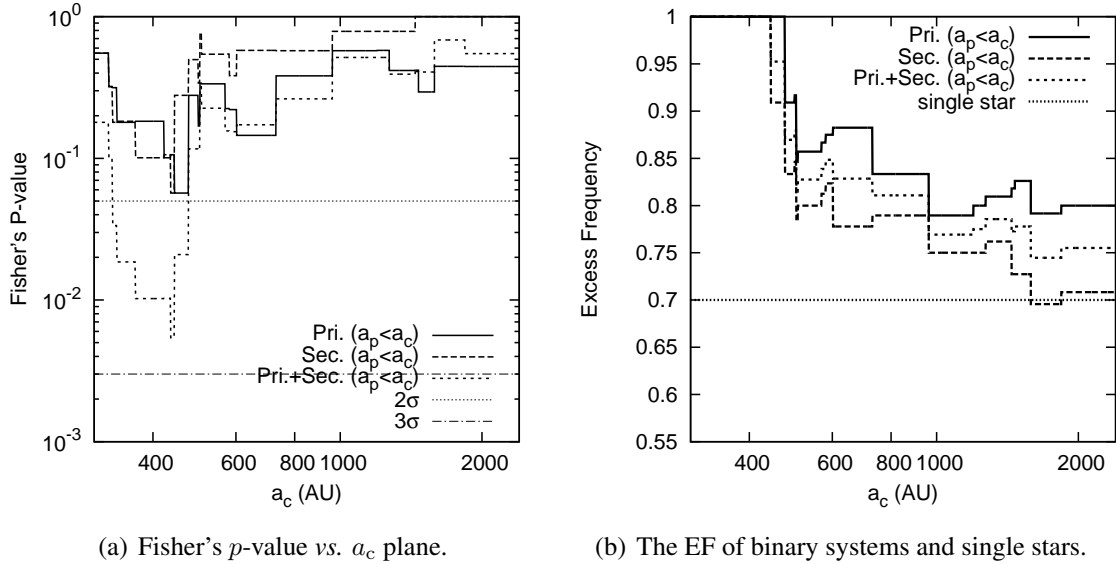
Figure 2.8: The figure is the same as Figure 6, but the comparison was performed between *closer binary systems* ($a_p < a_c$) and *single stars with calibration on putative tight companions*. (a): Fisher's *p*-value *vs.* a_c plane. The *horizontal-dotted* and *dashed-dotted* lines indicate the 2σ and 3σ levels, respectively. The *p*-value is minimized at $\sim$450 AU, where the difference in EF between binary systems with $a_\mathrm{p} < a_\mathrm{c}$ and single stars becomes most significant (2–3σ for primary+secondary sources). (b): The EF of binary systems and single stars. The *horizontal-dotted* line indicates the $\mathrm{EF_{single}}$ (70%).

2.5 Discussion

2.5.1 EF Distribution as a Function of Disk Outer Radius

The EF of binary systems with projected separations closer than $\sim$450 AU (100%) exceeded that of both wider systems and single stars at the 2–3σ significance level. In binary systems, the outer edge of the circumstellar disk is predicted to be truncated and prevented from free expansion by a companion star (e.g., Artymowicz & Lubow 1994). This truncated radius, R_{out}, strongly depends on the semi-major axis of the binary system a. On the other hand, disk dispersal timescale is governed probably by multiple stellar and disk properties, but it should at least be linked to the size of the disk. Therefore, the relationship between EF and a_{p} can be interpreted by R_{out}. We constructed a model of EF distribution as a function of R_{out}, $\mathrm{EF}_{\mathrm{model}}(R_{\mathrm{out}})$, to explore whether the characteristic disk size exists to explain the observed high EF at the projected separations of 280–450 AU. In the model, we divided the radial regions into three sections and assume a constant EF within one section. The radial ranges of the three regions and the EFs are treated as variables. To figure out the appropriate ranges of $\mathrm{EF}_{\mathrm{model}}$ and R_{out} for this model, we calculated $\mathrm{EF}_{\mathrm{model}}(a_{\mathrm{p}})$ through $\mathrm{EF}_{\mathrm{model}}(R_{\mathrm{out}})$ and compared it with the observed one, hereafter denoted as $\mathrm{EF}_{\mathrm{obs}}(a_{\mathrm{p}})$.

The relationship between a and a_{p} is given by

$$\frac{a}{a_{\mathrm{p}}} = \frac{(1 - e^2)[1 - \cos^2(\theta - \phi)\sin^2 i]^{0.5}}{1 + e\cos\theta} \tag{2.1}$$

, where θ, ϕ, i, and e denote the anomaly, reference angle, inclination, and eccentricity, respectively. To derive the a/a_{p} distribution, the eccentricity distribution is required. According to recent studies, the eccentricity distribution is relatively uniform (e.g., Raghavan et al. 2010; Dupuy & Liu 2011), and high-eccentricity ($e \gtrsim 0.8$) binaries are absent. Therefore, we assume a uniform eccentricity distribution ranging from $e = 0$ to 0.7. Using this eccentricity distribution, a peak appears at $a/a_{\mathrm{p}} = 1$ in the a/a_{p} distribution. In

the previous section, we measured $EF_{obs}(a_p \simeq 280\text{–}450 \text{ AU}) = 100\%$ and $EF_{obs}(a_p > 450 \text{ AU}) \simeq 70\%$; therefore, we expect that $EF_{model}(a \simeq 280\text{–}450 \text{ AU}) = 100\%$ and $EF_{model}(a > 450 \text{ AU}) \simeq 70\%$ would give a consistent EF distribution with the observations. In addition, $EF_{model}(a \lesssim 40 \text{ AU}) \sim 20\text{–}40\%$ is assumed based on the report by Cieza et al. (2009). Adopting a truncation radius of $R_{out} = 0.337a$ found in the systems of mass ratio $q \equiv M_p/M_s = 1$ with low-eccentricity (Pichardo et al. 2005), the EF can be estimated as a function of R_{out} over three separation regions; $R_{out} \lesssim 10 \text{ AU}$, $R_{out} \sim 100\text{–}150 \text{ AU}$, and $R_{out} \gtrsim 150 \text{ AU}$. From the above arguments, the values of the $EF_{model}(R_{out})$ in the three separation regions are varied around ~ 20, 100, and 70%, respectively. Between three regions, the EF is set by linear interpolation, as shown in Figure 2.9. The inner and outer limits of the radial region of $EF_{model}(R_{out}) \simeq 1$ are denoted as $R_{out;l}$ and $R_{out;h}$, respectively. We also define $R_{out;ch}$ and $R_{out;wl}$ as the outer boundary of the $EF_{model}(R_{out}) \simeq 0.2$ and the inner one of the $EF_{model}(R_{out}) \simeq 0.6$ region, respectively. From the relationship between EF_{model} and R_{out} determined from free parameters $\{R_{out;l}, R_{out;h}, R_{out;ch}, R_{out;wl}\}$ and values of the EFs in the three separation regions, we can derive $\{a_p, R_{out}, EF_{model}(a_p)\}$ from randomly selected binary orbital parameters $\{a, e, i, \theta, \phi\}$. The calculation assumes a uniform distribution of semi-major axes. This Monte Carlo approach allows us to compare the $EF_{model}(a_p)$ and $EF_{obs}(a_p)$ in order to determine the parameters related to the $EF_{model}(R_{out})$.

Figure 2.10 shows the results of the Monte Carlo computations obtained with $R_{out;l}$, $R_{out;h}$, $R_{out;ch}$, and $R_{out;wl}$ set to 30–40, 100, 10–20 AU, and 150–250 AU, respectively. The EFs of the three characteristic regions are 10% ($<R_{out;ch}$), 100% ($R_{out;l}$–$R_{out;h}$), and 70% ($>R_{out;wl}$). Although the flat EF regions shown in Figure 2.9 are smoothed by the projection effect, the EF remains high around $a_p \simeq 280\text{–}450 \text{ AU}$. In other words, the observed high EF region was reproduced when introducing this "peak" of EF into the model distribution. The model results *without* peaks are shown in the figure for comparison. For the model without a peak, we set $EF_{model}(>R_{out;l}) = 70\%$ so that the $EF_{model}(a_p)$ at larger a_p approaches the observed EF for wider binaries and single stars. We also set

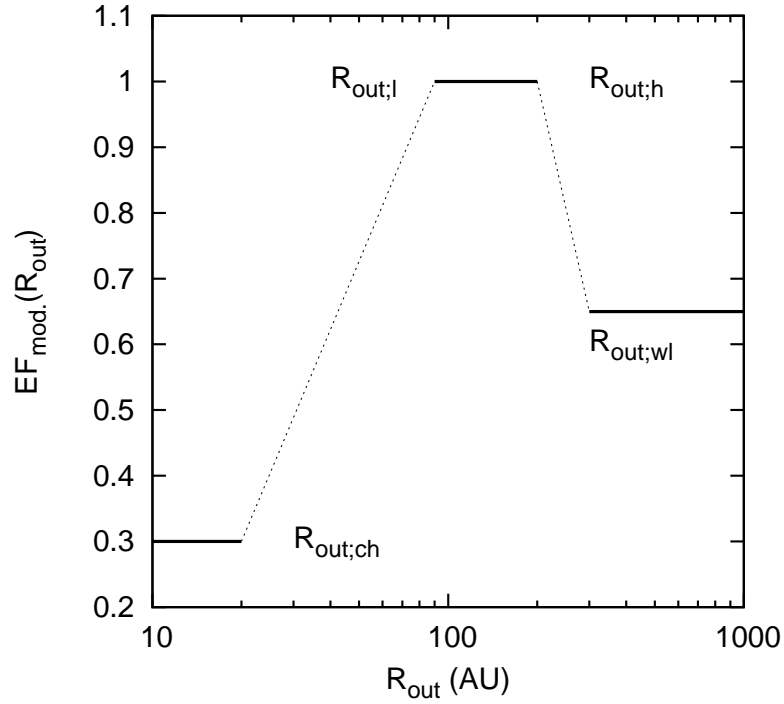Figure 2.9: Schematic of the $\mathrm{EF_{model}}(R_\mathrm{out})$ model. This figure shows one example case of three EFs. $R_\mathrm{out;ch}$ expresses the outer radius of the innermost EF region, where the EF is set to be similar as observed in binaries separated by less than $\sim$40 AU (Cieza et al. 2009). $R_\mathrm{out;l}$ and $R_\mathrm{out;h}$ represent the inner and outer limit of the high EF region, respectively. Introducing these two variables yields a "peak" in the EF distribution. $R_\mathrm{out;wl}$ represents the inner boundary of the outermost EF region. The three regions are linearly connected (*dotted* lines in the figure).
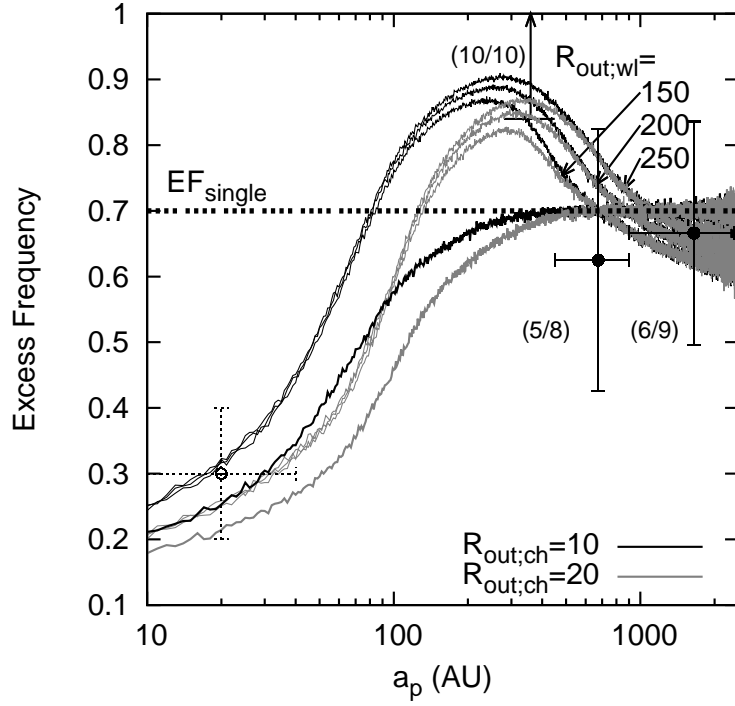
Figure 2.10: $\text{EF}_{\text{model}}(a_{\text{p}})$ derived from $\text{EF}_{\text{model}}(R_{\text{out}})$. *Black* and *gray solid* lines denote $R_{\text{out;ch}} = 10$ and 20 AU, respectively. In the peak model, the EF at wide binary separations ($a_{\text{p}} \gtrsim 100$) depends on $R_{\text{out;wl}}$. The selected parameter values are indicated in this figure. If no peak is present in the distribution, the EF is almost flat at wide separations. The observational EF data for primary sources are shown for comparison. Error bars represent the 1σ confidence interval estimated from the binomial distribution. As reference, the EF of a closely spaced binary ($<$40 AU, from Cieza et al. 2009) is plotted with dotted error bars. The *dotted horizontal* line represents the EF of a single star (see Section 2.4.3).

$EF_{model}(R_{out;ch})$=10–20% so that the EF of the inner 40 AU is consistent with the observed one, 20–40% (Cieza et al. 2009). These results disagree with the observational data around $a_p \simeq$ 280–450 AU (Figure 2.10).

The separation-dependent distribution was investigated individually for excess and non-excess sources, by a Kolmogorov-Smirnov (K-S) test. We iteratively sampled $\sim 10^4$ sources from the $EF_{model}(R_{out})$ at the same a_p as the observed binary, and counted the number of excess or non-excess objects at each a_p. In this way, our model predicts how many sources show and do not show excess at a_p and their cumulative distribution functions (CDF). According to the K-S test, the model predicts the separation-dependent distribution of both primary and secondary excess sources, regardless of whether the peak is included in the model. However, for sources that do not show excess, the model predictions disagree with observations when the peak is excluded. As shown in Figure 2.11, $p \gtrsim 0.32$ is obtained by the K-S test where p is the probability that the observed binary sources (primary plus secondary) are drawn from the same parent sample as the model *with* an EF peak. On the other hand, p-value is $\lesssim 0.1$ for the model without a peak, suggesting disagreement with the observations. Therefore, although it is not statistically significant, the peak-ed EF_{model} is more consistent with the observed result than the flat EF_{model}. We discuss the interpretation of the EF peak seen in $a_p \simeq$ 280–450 AU and attempt to explain why the EF of this separation range is higher compared to that of the single stars in the next section.

2.5.2 Mechanism of Dust Dispersal in Binary Systems

The EFs of primary and secondary sources in our sample separated by $a_p \simeq$ 280–450 AU are $100^{+0}_{-17}\%$ and $91^{+8}_{-18}\%$, respectively. At wider separations, the EF reduces to that of single stars (70 ± 5%). On the other hand, the EF of close binaries ($a_p \sim$ 10–40 AU) has been previously determined as $\sim$20–40% (Cieza et al. 2009). In the previous section, we expressed the separation-dependent EF in terms of R_{out}. The EF significantly decreases
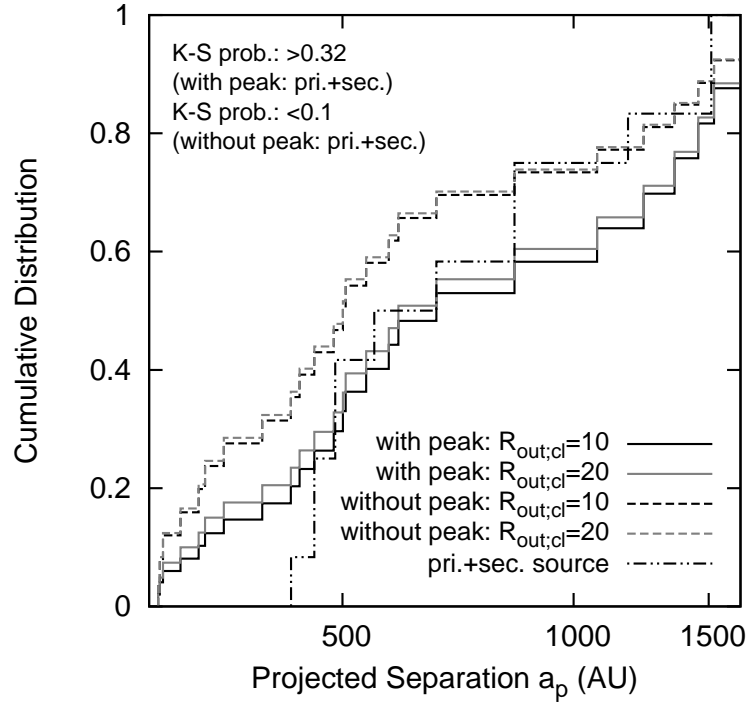
Figure 2.11: Cumulative distributions of the projected separation, a_{p}. As demonstrated by the K-S tests, if the "peak" is excluded from the $\mathrm{EF}_{\mathrm{model}}(R_{\mathrm{out}})$ distribution, discrepancy appears between the predicted and the observed separation-dependent EF distribution. *Solid* and *dashed* lines show the results with and without the peak in the model, respectively. *Black* and *gray* colors denote the calculations assuming $R_{\mathrm{out;ch}} = 10$ and 20, respectively. The observed distribution is indicated by the *dash-two-dotted* line.

and increases relative to that of single stars when $R_{\mathrm{out}} \lesssim 10$ AU and $R_{\mathrm{out}} \sim 30$–100 AU, respectively, and matches the single star value at $R_{\mathrm{out}} \gtrsim 150$ AU. This brings us to the implication: *the time scale of dust dissipation might be prolonged in disks of characteristic radius ($\sim$30–100 AU)*. This disk size is smaller than the size estimated for single stars, reported as $\sim$200 AU (e.g., Andrews & Williams 2007) and $\sim$100–1100 AU (Schaefer et al. 2009, and references therein). Given that the EF is reduced in wide binary systems ($\gtrsim$450 AU, thus $R_{\mathrm{out}} \gtrsim 150$ AU), we speculate that extended disks (greater than $\sim$30–100 AU) undergo significant mass loss in the outer disk region.

Various mechanisms of gas and dust removal have been proposed, including viscous evolution, planetesimal growth, photoevaporation, disk wind induced by magnetorotational instability, and sculpting by planets (e.g., Williams & Cieza 2011; Suzuki et al. 2010). In viscous evolution, the timescale of dissipation is given by $t \propto R_{\mathrm{out}}^2$. The R_{out} of binary systems depends upon the semi-major axis a, being approximated by $\sim a/3$ (e.g., Artymowicz & Lubow 1994; Pichardo et al. 2005). Therefore, the peak in the EF distribution is difficult to reproduce assuming viscous evolution alone, since more time is required to disperse the dust disk as the binary separation (hence the disk size) increases.

Disk photoevaporation is a well-known mechanism and may successfully explain the actual disk dispersal (e.g., Hollenbach et al. 1994; Clarke et al. 2001; Alexander & Armitage 2007). Ionizing flux from the central star creates a disk thermal wind and material beyond the critical radius can escape the disk as the gravitational potential weakens. On the other hand, viscous accretion continues, leaving an inner hole within the critical radius due to the lack of sufficient mass supply from the outer region and the short timescale of viscous process at small radii. Armitage et al. (2003) considered the photoevaporation in their study of disk evolution in binary systems. In their modeling work, the disk lifetime in a binary depended on its separation, and the maximum lifetime was predicted at $\sim$15–100 AU, depending on the model which they used. They speculated that binary systems with those intermediate separations have less area where the disk mass can be lost by photoevaporative wind and to moderately counteract the disk dispersal. This earlier

prediction cannot be verified by the results presented here because we cannot ascertain whether the sources with no IRAC excess really lack outer disks without analyzing the longer wavelengths data. However, it is worth pointing out that the EF distribution has a peak in the intermediate separation range also in our study. This similarity between the observed result and the theoretical prediction implies that photoevaporation has a possibility to be one of the effective mechanisms controlling the disk evolution in binary systems.

Disk lifetime is related also to disk mass. If we assume the disk dispersion described above, among the binaries of $a_p \gtrsim 280$ AU, the closer binaries ($a_p < 450$ AU) should have heavier disks than the wider binaries ($a_p > 450$ AU). However, such a trend has not been found so far. Binaries separated by >280 AU are speculated to have the same degree of millimeter luminosity, in other words, the same disk mass as single stars (Harris et al. 2012). Unfortunately, it is still difficult to statistically confirm the change in disk mass within a narrow separation range of ~ 280–500 AU.

There is another possibility to interpret the dependence of EF on binary separation. Systems with wider separations tend to be triples or quadruples. If the 450 AU represent the boundary beyond which binaries become sufficiently wide that they start to have additional higher-order components, and they harbor close companions, the decreasing of EF can be accounted for by an increasing of existence of multiple systems. In order to clarity this possibility, a larger sample is needed for wide binaries for which the presence of close companions were thoroughly investigated.

To explain the prolonged disk-dissipation timescale in the disks of characteristic radius ($\sim$30-100 AU), Figure 2.12 shows another concept for photoevaporation mechanism. Because the closely separated binary systems should have small disk radii, their disks consequently accrete onto the central star, that is, primary or secondary stars within short time. In these closely separated binary systems, there should be a massive circumbinary disk (Figure 2.12 (a)). Theoretical results suggest that a circumbinary disk can transfer mass onto circumstellar disks, i.e., circumprimary or circumsecondary disks, through

nonaxisymmetric structures (gas arms). However, the size of circumstellar disks might be too small to overcome the disk dissipation even if mass transfer from circumbinary to circumstellar disks exists. In wide binary systems, the circumstellar disks are larger and the photoevaporated gas is rapidly swept away from the outer region of the circumstellar disks. However, when a circumbinary disk exists, the photoevaporated gas might be possibly captured by the circumbinary disk. Consequently, the lifetime of the circumstellar disk is prolonged by the mass transfer from the circumbinary to circumstellar disks (Figure 2.12 (b)). Furthermore, if the binary separation expands, because no existing circumbinary disks capture the photoevaporated gas from circumstellar disks, there is no resupply mechanism for the photoevaporated gas captured by the circumbinary disk to the circumstellar disk (Figure 2.12 (c)). As a result, in binary systems with significantly large separation, the lifetime of circumstellar disks degreases.
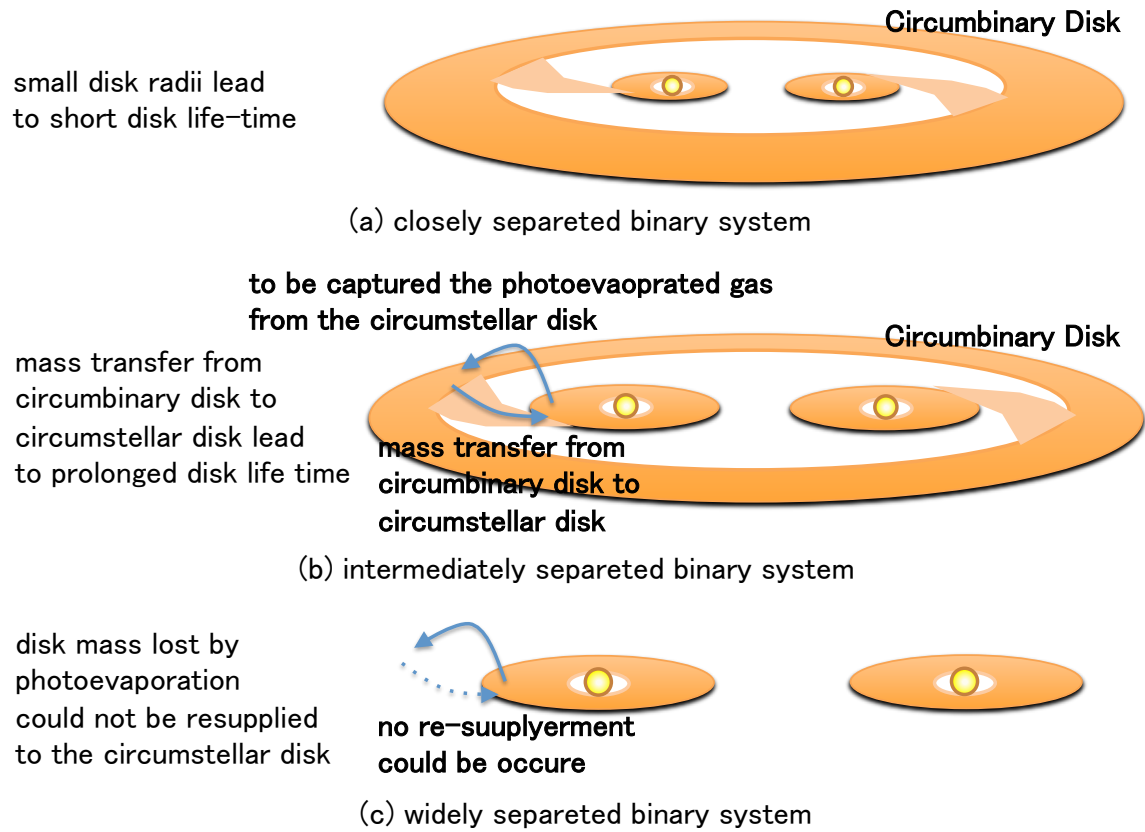
Circumbinary Disk

small disk radii lead
to short disk life–time

(a) closely separeted binary system

to be captured the photoevaoprated gas
from the circumstellar disk

Circumbinary Disk

mass transfer from
circumbinary disk to
circumstellar disk lead
to prolonged disk life time

mass transfer from
circumbinary disk to
circumstellar disk

(b) intermediately separeted binary system

disk mass lost by
photoevaporation
could not be resupplied
to the circumstellar disk

no re–suuplyerment
could be occure

(c) widely separeted binary system

Figure 2.12: The photoevaporation mechanism explaining the prolonged disk-dissipation timescale in disks of the characteristic radius ($\sim$30-100 AU). The diagrams show (a) closely separated binary systems, (b) moderately separated binary systems ($R_{out} \sim 30 - 100$ AU), and (c) significantly separated binary systems.

2.6 Conclusion

Using archival data obtained by *Spitzer*/IRAC, infrared excess emission was investigated for 27 binary systems in two nearby star-forming regions, Taurus and Ophiuchus. Our sample consisted of binaries with projected separations of $2''.0$–$17''.0$ ($\simeq$280–2400 AU), enabling the study of circumstellar disks associated with individual binary components.

After excluding Class I and objects that cannot be young, spatially resolved photometry yielded the following results for 24 binaries or 51 primary and secondary sources.

1. The excess frequency (EF) of *all* primary and secondary stars based on $[3.6] - [8.0]$ color is indistinguishable from that of single stars (70$\pm$5%). This result is consistent with past studies in which the disk frequency of wide binary systems ($\gtrsim$100 AU) is not significantly different from that of single stars. The sources showing excess emission at 8.0 μm also exhibits excess at the shorter wavelengths. Conversely, sources without excess at 8.0 μm are photospheric at the other IRAC wavelengths. The exceptions are three sources that show excess at 8.0 μm but not in one or more shorter wavebands.

2. In four systems out of 24 (17^{+11}_{-8}%), excess emission is shown by either the primary or secondary component (designated "mixed" systems). In one of these mixed systems, excess is found only for the secondary star. No significant preference for either the circumprimary or circumsecondary disk to disperse is found. However, the rareness of mixed systems suggests that dust dispersal is strongly correlated between the two disks, even at the binary separations exceeding $\gtrsim$280 AU.

3. The EFs of closely and widely spaced binary systems are different, with the two groups divided at $a_{\rm p} \sim$450 AU. For the entire sample (including both primary and secondary sources), this difference is significant at the 2–3σ level. The EF of primary and secondary sources separated by less than 450 AU was 100^{+0}_{-17}% and 91^{+8}_{-18}%, respectively. This high EF was compared with that of single stars within

a similar range of luminosity and spectral type (i.e., similar age and mass). The Fisher's exact test shows that the maximum EF ($\sim$100%) is higher than that of single stars with a significance of $\gtrsim$2–3σ for three kinds of binary sample consisting of primary or secondary or both components.

Comparing the predicted separation-dependence of the EF distribution with the observational data, the model requires a high EF region ("peak") around R_{out} $\sim$30–100 AU as confirmed by the K-S test. This disk size is smaller than the typical one estimated for single stars, implying that the dissipation of moderately truncated circumstellar disks is prolonged. The EF of widely-spaced binary systems, presumably with larger circumstellar disks, is indistinguishable from that of single stars. Our result is consistent with the prediction that extended disks may suffer from significant mass loss in the outer regions by photoevaporation (Armitage et al. 2003), suggesting that photoevaporation contributes to the evolution of circumstellar disks in binary systems.

Chapter 3

IMPLICATIONS FOR PLANET FORMATION IN BINARY SYSTEMS

As described in Section 1, there are two well known mechanisms to describe the formation of giant planets: core accretion (Pollack et al. 1996) and gravitation instability (Toomre 1964; Boss 2000). One of the major differences between the two mechanisms is prediction of the timescale of planet formation. Core accretion requires more than several Myr to build a Jupiter-sized planetary core (e.g., Hubickyj et al. 2005; Dodson-Robinson et al. 2008). The planet forms in a few hundred years or less when the disk becomes gravitationally unstable. Planets are expected to form via a similar mechanism in binary systems.

If the disks, which are prone to gravitational instability, form planets, dust dispersal is then enhanced. Consequently, these disks will be observed as nonexcess sources in IRAC bands. However, the results in this study disagree with the accelerated dust dispersal. Considering long-lived disks within binary systems with a separation of ~ 280–400 AU, these binary systems are reasonable planet-forming sites via core accretion.

Figure 3.1 shows the planet mass distribution ($M_p \sin i$) in binary systems as a function of the binary separation. We used planet samples associated with binary systems from Roell et al. (2012). The horizontal dotted line represents the median and average mass of

all known extrasolar planets to date. Planets heavier than the average mass in binaries with $a_p \sim 200$–500 AU are somewhat less frequent than expected based on the distribution of planets in either wide or close binaries. Considering the high EF, and the prolonged disk lifetime within this binary separation range, such binary systems may form planets via core accretion process. Nevertheless, core accretion requires more than several Myr to build a Jupiter-sized planetary core and this timescale is longer than the disk dissipation timescale of a few Myr by one digit. Consequently, massive planets in binaries with $a_p \sim 200$–500 AU might be less common. In wide binaries ($a_p \sim 1000$ AU), planets covering two orders of magnitude can be observed and it is speculated that these planets did not form via a single mechanism. In tight binaries with short disk lifetimes, planet formation via core accretion is unlikely, especially if the planets are particularly massive. Indeed, planets located within less than $\sim$100 AU lack low-mass gas giants with $<2M_J$. As described above, the dependence of planet mass on binary separation might be divided into three separation regions. Although the small number of planets and high possibility of existing the sample bias prevent the investigation of the correlation between the EF and planet mass, similar behavior observed in the EF is of great interest.

The disk lifetime and sizes around single stars have been derived from previous surveys of many clusters. The detection of several thousands of planets has also shown the distribution of planet masses around single stars. However, the absence of companions does not prevent the disk from expanding freely and it leads to large dispersion in disk sizes. Additionally, speculating on the original disk sizes or lifetime for each planet-hosting star is difficult. Therefore, obtaining the relation between planet mass and disk radius (or disk lifetime) from single stars is difficult. On the other hand, the gravitational torque from the companion truncates the disk (Paczynski 1977) and prevents it from expanding freely. From previous observational studies, it has been clarified that most disks ($\sim$60%) within binary systems are amenable to theoretically predicted disk size (e.g., Harris et al. 2012). The above argument implies that identifying the consistency between "separation vs. disk lifetime" and "separation vs. planet mass" can via observations
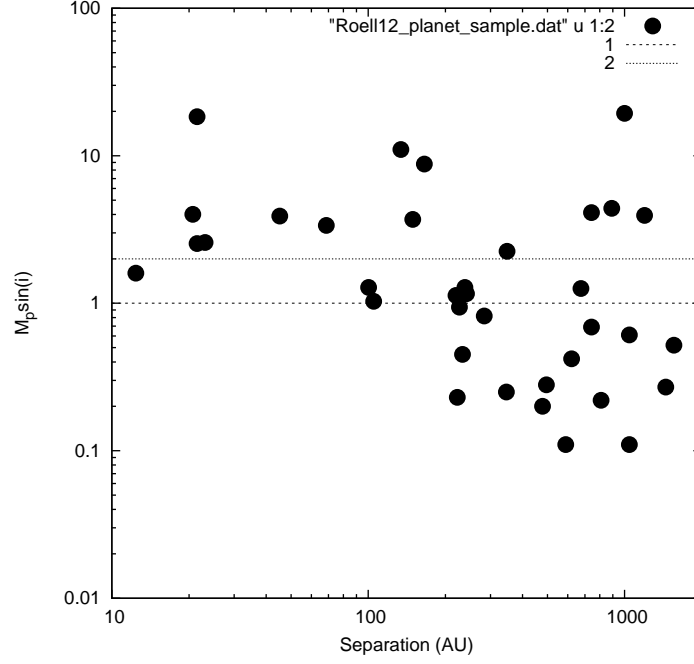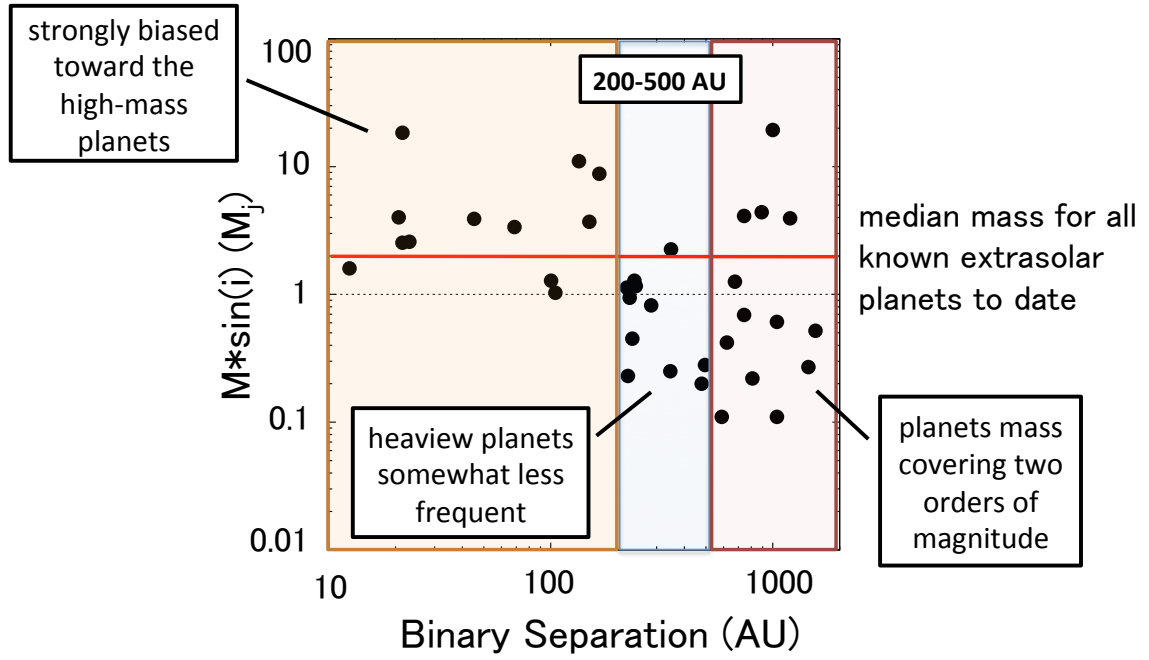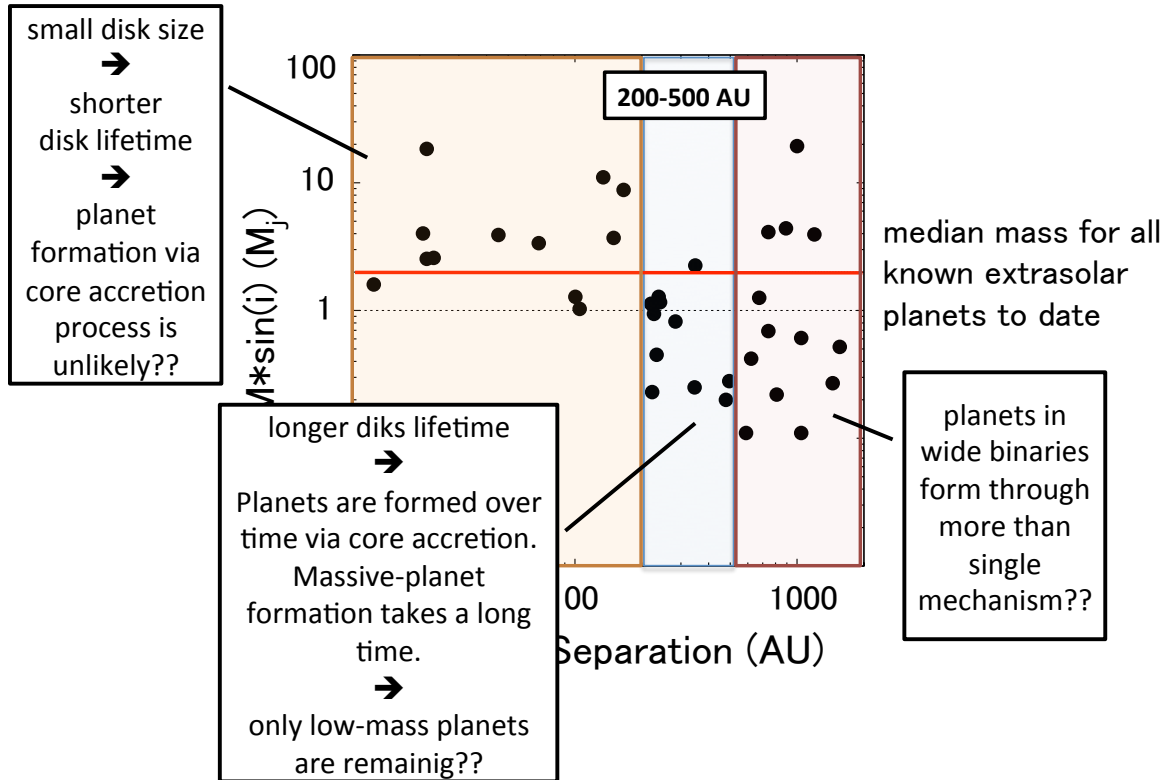
Figure 3.1: Planet mass distribution ($M_p \sin i$) in binary systems as a function of the binary separation. Note the lack of planets with $M_p \sin i = M_J$ for binaries tighter than 100 AU. The horizontal dotted line represents the median mass for all known extrasolar planets to date (including among single stars).

constrain the formed planet masses depending on the disk lifetime, i.e., disk sizes (Figure 3.2). Binary systems would be the most appropriate site to determine the correlation between disk lifetime and the resulting planet mass. The result of this study sheds light to this correlation. To increase the resolution of the dependency of the disk lifetime on binary separation in the wide separation range and to derive the correlation between the disk lifetime and disk radius (separation) in each region, more samples are required. Furthermore, as mentioned above, to constrain the correlation between the formed planet mass and disk radius and lifetime, additional studies are required for planets within binary systems.

(a) Three characteristic regions in the distribution of masses ($M_p \sin i$) for planets in binary systems

(b) Interpretation of the planet formation mechanism within each characteristic region

Figure 3.2: Three characteristic regions in the planet mass distribution ($M_p \sin i$) in binary systems (a) and interpretation of the planet formation mechanism in each region (b).
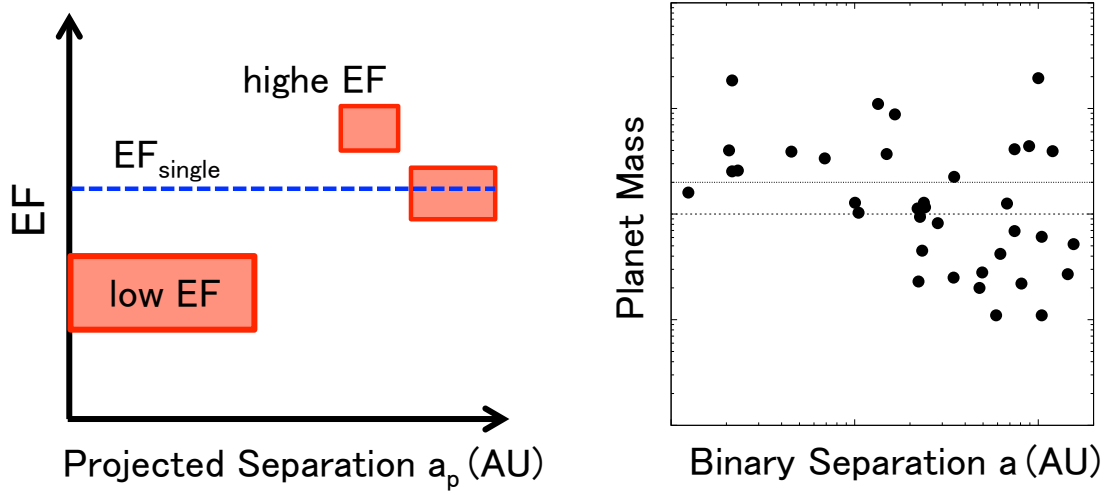
Figure 3.3: Relation between "separation vs. EF (disk lifetime) " (*left*) and "separation vs. planet mass" (*right*). Identifying the consistency between "separation vs. disk lifetime" and "separation vs. planet mass" can constrain via observation the formed planet masses depending on the disk lifetime (i.e., disk sizes).

Acknowledgments

References

Abt, H. A., & Levy, S. G. 1976, ApJ, 30, 273

Akeson, R. H., & Jensen, E. L. N. 2014, ApJ, 784, 62

Alexander, R. D., & Armitage, P. J. 2007, MNRAS, 375, 500

Allard, F., Hauschildt, P. H., Alexander, D. R., et al. 2001, ApJ, 556, 357

Allers, K. N., Kessler-Silacci, J. E., Cieza, L. A., & Jaffe, D, T. 2006, ApJ, 644, 364

Andrews, S. M., & Williams, J. P. 2007, ApJ, 659, 705

Armitage, P. J., Clarke, C. J., & Palla, F. 2003, MNRAS, 342, 1139

Artymowicz, P., & Lubow, S. H. 1994, ApJ, 421, 651

Baraffe, I., Chabrier, G., Allard, F., & Hauschildt, P. H. 1998, A&A, 337, 403

Bessell, M. S., & Brett, J. M. 1988, 100, 1134

Bontemps, S., André, P., K. A. A., et al. 2001, A&A, 372, 173

Bouwman, J., Lawson, W. A., Dominik, C., et al. 2006, ApJ, 653

Chavarría K, C., Terranegra, L., Moreno-Corral, M. A., & de Lara, E. 2000, 145, 187

Cieza, L. A., Padgett, D. L., Allen, L. E., et al. 2009, ApJ, 696

Clarke, C. J., Gendrin, A., & Sotomayor, M. 2001, MNRAS, 328, 485

Connelley, M. S., & Greene, T. P. 2010, AJ, 140, 1214

Correia, S., Zinnecker, H., Ratzka, T., & Sterzik, M. F. 2006, A&A, 459, 909

Currie, T., & Sicilia-Aguilar, A. 2011, ApJ, 732, 24

Cutri, R. M., Skrutskie, M. F., van Dyk, S., et al. 2003

Daemgen, S., Correia, S., & Petr-Gotzens, M. G. 2012, A&A, 540, 46

Delfosse, X., Beuzit, J.-L., Marchal, L., et al. 2004, 318, 166

Duchêne, G. 1999, A&A, 341, 547

Duchêne, G., Bontemps, S., André, P., et al. 2007, A&A, 476, 229

Duchêne, G., Monin, J.-L., Bouvier, J., & Ménard, F. 1999, A&A, 351, 954

Dupuy, T. J., & Liu, M. C. 2011, ApJ, 733, 122

Duquennoy, A., & Mayor, M. 1991, A&A, 248, 485

Evans, N. J., I., Allen, L. E., Blake, G. A., et al. 2003, 115, 965

Evans, N. J., I., Dunham, M. M., Jørgensen, J. K., et al. 2009, ApJS, 181, 321

Fazio, G. G., Hora, J. L., Allen, L. E., et al. 2004, ApJS, 154, 10

Fischer, D. A., & Marcy, G. W. 1992, ApJ, 396, 178

Furlan, E., Luhman, K. L., Espaillat, C., et al. 2011, ApJS, 195, 3

Ghez, A. M., Neugebauer, G., & Matthews, K. 1993, AJ, 106, 2005

Grankin, K. N., Melnikov, S. Y., Bouvier, J., et al. 2007, A&A, 461, 183

Greene, T. P., & Meyer, M. R. 1995, ApJ, 450, 233

Haisch, Jr., K. E., Barsony, M., Greene, T. P., & Ressler, M. E. 2002, AJ, 124, 2841

REFERENCES

Haisch, Jr., K. E., Greene, T. P., Barsony, M., & Stahler, S. W. 2004, AJ, 127, 1747

Harris, R. J., Andrews, S. M., Wilner, D. J., & Kraus, A. L. 2012, ApJ, 751, 115

Hartigan, H., & Kenyon, S. J. 2003, ApJ, 583, 334

Herbig, G. H., & Bell, K. R. 1988, 90

Hollenbach, D., Johnstone, D., Lizano, S., & Shu, F. 1994, ApJ, 428, 654

Indebetouw, R., Mathis, J. S., Babler, B. L., et al. 2005, ApJ, 619, 931

Kenyon, S. J., & Hartmann, L. 1995, ApJS, 101, 117

Köhler, R., & Leinert, C. 1998, A&A, 331, 977

Koornneef, J. 1983, A&A, 128, 84

Kraus, A. L., & Hillenbrand, L. A. 2007, ApJ, 662, 413

—. 2009a, ApJ, 704, 531

—. 2009b, ApJ, 703, 1511

Kraus, A. L., Ireland, M. J., Hillenbrand, L. A., & Martinache, F. 2012, ApJ, 745, 19

Kraus, A. L., Ireland, M. J., Martinache, F., & Hillenbrand, L. A. 2011, ApJ, 731, 8

Kurucz, R. L. 1993

Lada, C. J. 1987, 115, 1

Lada, C. J., & Adams, F. C. 1992, ApJ, 393, 278

Leinert, C., Zinnecker, H., Weitzel, N., et al. 1993, A&A, 278, 129

Loinard, L., Torres, R. M., Mioduszewski, A. J., & Rodríguez, L. F. 2008, 675

Luhman, K. L., Allen, P. R., Espaillat, C., et al. 2010, ApJS, 186, 111

Luhman, K. L., & Rieke, G. H. 1999, ApJ, 525, 440

Mamajek, E. E. 2009, 3

Martin, P. G., & Whittet, D. C. B. 1990, ApJ, 113

Mathieu, R. D., Walter, F. M., & Myers, P. C. 1989, AJ, 98, 987

Mayama, S., Tamura, M., Hanawa, T., et al. 2010, 327, 306

McCabe, C., Ghez, A. M., Prato, L., et al. 2006, ApJ, 636, 932

McClure, M. K., Furlan, E., Manoj, P., et al. 2010, ApJS, 188, 75

Meyer, M. R., C. N., & Hillenbrand, L. A. 1997, Aj, 114, 288

Monet, D. G., Levine, S. E., Canzian, B., et al. 2003, AJ, 125, 984

Moneti, A., & Zinnecker, H. 1991, A&A, 242, 428

Monin, J.-L., Clarke, C. J., Prato, L., & McCabe, C. 2007

Monin, J. L., Ménard, F., & Duchêne, G. 1998, A&A, 330, 310

Neuhaeuser, R., S. M. F. S. J. H. M. M. W. R., & Krautter, J. 1995, A&A, 297, 391

Pichardo, B., Sparke, L. S., & Aguilar, L. A. 2005, MNRAS, 359, 521

Prato, L., Greene, T., P., & Simon, M. 2003, ApJ, 584, 853

Prato, L., & Simon, M. 1997, ApJ, 474, 455

Raghavan, D., McAlister, H. A., Henry, T. J., et al. 2010, ApJS, 190, 1

Ratzka, T., Köhler, R., & Leinert, C. 2005, A&A, 437, 611

Rebull, L. M., P. D. L. M. C.-E., et al. 2010, ApJS, 186, 259

Reipurth, B., & Zinnecker, H. 1993, A&A, 278, 81

REFERENCES

Roell, T., Neuhˊauser, R., Seifahrt, A., & Mugrauer, M. 2012, A&A, 542, 92

Sestito, P., Palla, F., & Randich, S. 2008, A&A, 487, 965

Simon, M., Ghez, A. M., & Leinert, C. 1993, 408

Suzuki, T. K., Muto, T., & Inutsuka, S.-i. 2010, ApJ, 718, 1289

Torres, C. A. O., Quast, G. R., da Silva, L., et al. 2006, A&A, 460, 695

Torres, R. M., Loinard, L., Mioduszewski, A. J., & Rodríguez, L. F. 2007, ApJ, 671, 1813

Wahhaj, Z., Cieza, L., Koerner, D. W., et al. 2010, ApJ, 724, 835

Walter, F. M., Vrba, F. J., Mathier, R. D., et al. 1994, AJ, 107, 692

White, R. J., & Ghez, A. M. 2001, ApJ, 556, 265

White, R. J., & Hillenbrand, L. A. 2004, ApJ, 616, 998

Wichmann, R., Torres, G., Melo, C. H. F., et al. 2000, A&A, 359, 181

Wilking, B. A., Meyer, M. R., Robinson, J. G., & Greene, T. P. 2005, AJ, 130, 1733

Williams, J. P., & Cieza, L. A. 2011, 49, 67

Yi, S., Demarque, P., Kim, Y.-C., et al. 2001, ApJS, 136, 417

Zacharias, N., Monet, D. G., Levine, S. E., et al. 2005

Appendix A

Notes on Individual Binaries

A.1   2MASS J16263682-2415518 B

This binary system is located in Ophiuchus. The secondary star begins exhibiting significant excess (0.48 ± 0.14 mag) at 8.0 μm. The binary separation is very wide at $9\rlap{.}''08$ (Duchêne et al. 2007), and the spectral type of the secondary star is estimated as M5 (Wilking et al. 2005).

The SED fitting was performed to the flux density in R, I, and J bands obtained from USNO-B1 and 2MASS Catalog. Significant excess emission was confirmed at 8.0 μm, but was not identified at 5.8 μm. However, the possible excess at 5.8 μm might have been underestimated because the photometric values at 3.6 and 4.5 μm are smaller than the fitted photosphere. The measured color of $[4.5] - [5.8]$ (0.49 ± 0.2 mag) is in fact significantly higher than the photospheric color for an M5-type star (0.04 mag; Luhman et al. (2010)), thus excess emission likely begins at 5.8 μm. The discrepancy between the photometry and the fitted photospheric values at 3.6 and 4.5 μm could arise from the poor SED fitting due to the faintness of the object in the R band (19.2 mag). Therefore, according to its color, we consider that this object has an onset of the excess at $\sim$5.8–8.0 μm.

The source was detected at 24 μm in the c2d survey, and the photometric value of

5.71±0.19 mag was provided in the catalog. The $[8.0]-[24]$ color is then 3.46 ± 0.24 mag, which is significantly higher than the photospheric one for an M5-type star (0.23 mag; Luhman et al. (2010)). Thus, we again confirmed the existence of circumsecondary dust, and the occurrence of dust dispersion in the inner region of the disk.

A.2   V710 Tau A

The binary separation of V710 Tau is $3\overset{''}{.}0$ (White & Ghez 2001). The spectral types of the primary and secondary stars are estimated as M0.5 and M2, respectively (White & Ghez 2001). In V710 Tau, excess emission is found only for the primary source. The subtraction of the photospheric model derived from the SED fitting resulted in significant excess at 5.8 and 8.0 μm, with values of 0.37 ± 0.14 and 0.94 ± 0.14 mag, respectively. On the other hand, no excess was observed at 3.6 and 4.5 μm. The $[4.5] - [5.8]$ color of 0.67 ± 0.2 mag is significantly higher than the photospheric color of 0.2 mag, also suggesting that excess emission begins from 5.8 μm. In other wavebands, the primary star shows a small excess in L band ($K - L = 0.44$; White & Ghez (2001)) and a substantial one in N ($K - N = 3.32$; McCabe et al. (2006)). The significant excess starting from 5.8 μm is not inconsistent with these previous studies.

The flux density at 24 μm was obtained as 236 mJy for the whole system (primary plus secondary) (Wahhaj et al. 2010). The magnitudes measured at 8.0 and 24.0 μm for the system are 6.30 ± 0.20 mag and 3.71 ± 0.11 mag, respectively, then the color of $[8.0]-[24]$ is 2.59 ± 0.23 mag. This is significantly larger than an averaged-photospheric color of an M-type star of 0.22 mag (Luhman et al. (2010)). Because the emission at 24 μm cannot be spatially resolved, it is difficult to conclude whether the origin of the emission is circumprimary, circumsecondary, both of them, or circumbinary disks. However, considering the separation of ~ 280 AU, the emission at 24 μm is possibly not from the inner edge of a circumbinary disk.

A.3   JH 223 A

The binary JH 223 belongs to the Taurus region. The primary star of this system shows the significant excess at 4.5 μm. The binary separation is small ($2\rlap{.}''07$; Kraus et al. (2011)), and the spectral types of its primary and secondary are estimated as M2 and M6.5, respectively (Kraus & Hillenbrand 2007).

The excess emission at 3.6, 4.5, 5.8, and 8.0 μm were -0.04 ± 0.03, 0.33 ± 0.04, 0.61 ± 0.04, and 1.03 ± 0.04 mag, respectively, estimated by subtracting the photospheric magnitudes obtained from the SED fitting. This indicates that the onset of the excess is at around 4.5 μm. The resultant $\chi^2/\mathrm{d.o.f.}$ values for the PSF fitting photometry were 1.0, 0.4, 0.7 and 1.0 at the four wavelengths, respectively, implying that the fitting was reasonably performed. The Hα emission have identified this source as a Weak-lined T Tauri Star (Neuhaeuser & Krautter (1995) and references therein), suggesting that this source lacks an optically-thick, inner disk with active accretion, but may possess an optically-thick, exterior disk.

The photometry at 24 μm was previously obtained as 5.13 ± 0.04 mag for the primary and secondary sources (Rebull et al. 2010). The measured magnitudes at 8.0 μm of the system is 7.72 ± 0.20 mag and the $[8.0] - [24]$ color is calculated to be 2.59 ± 0.20 mag, which is significantly higher than an averaged-photospheric value of an M-type star of 0.22 mag (Luhman et al. 2010). As in the case of V710 Tau, although it is hard to conclude the origin of the excess emission, the emission at 24 μm may not be caused by the circumbinary disk.

Appendix B

# Estimation of the Upper Brightness Limit of Undetected Secondaries of DoAr 24 E

In the image of DoAr 24E at 3.6 μm, we could not resolve and obtain the photometry of the secondary star due to its separation (2$\overset{''}{.}$07) and faintness (large contrast to brightness of the primary star). We attempted to estimate the upper brightness limit of the undetected secondary star in the observed image at 3.6 μm. To do so, we first added an artificial secondary star at P.A. 180 degrees away from the actual source. We assumed that the position of the actual secondary star corresponded to the average position, which was obtained from other wavelength data. Second, we tried to resolve the primary star and artificial secondary star using our resolving tool (described in the draft paper) under assumption that the brightness of actual secondary star dose not affects the resolving process. Therefore, we only used "two" stellar profiles, one for the primary and the other for the artificial secondary star. We estimate the upper limit of the brightness of the artificial secondary star by altering its brightness.

Figure B.1 shows the result of the analysis discussed above. For the faint brightness of the artificial secondary star (the value of horizontal axis is ∼9.5-8.2 mag), the discrepancy

between the model brightness, which is the image of the primary and artificial secondary sources, and the detected value of the secondary star is tenfold. The reason is discussed below. The procedure for resolving this was conducted by altering the scales and positions of the two stellar profiles for the primary and secondary sources. If the brightness of the artificial secondary star is sufficiently faint, the stellar profile of the secondary star located near the position of the primary star satisfies the minimum value of χ^2. Therefore, the brightness of the secondary star detected within this brightness region cannot reflect the embedded artificial secondary star.

Once the brightness of the artificial secondary star is $\gtrsim 8.2$, the turning point in the profile of the secondary star can be used to detect the artificial secondary star (see Fig. B.1.). We can confirm the decreasing discrepancy with increasing brightness of the artificial secondary star.
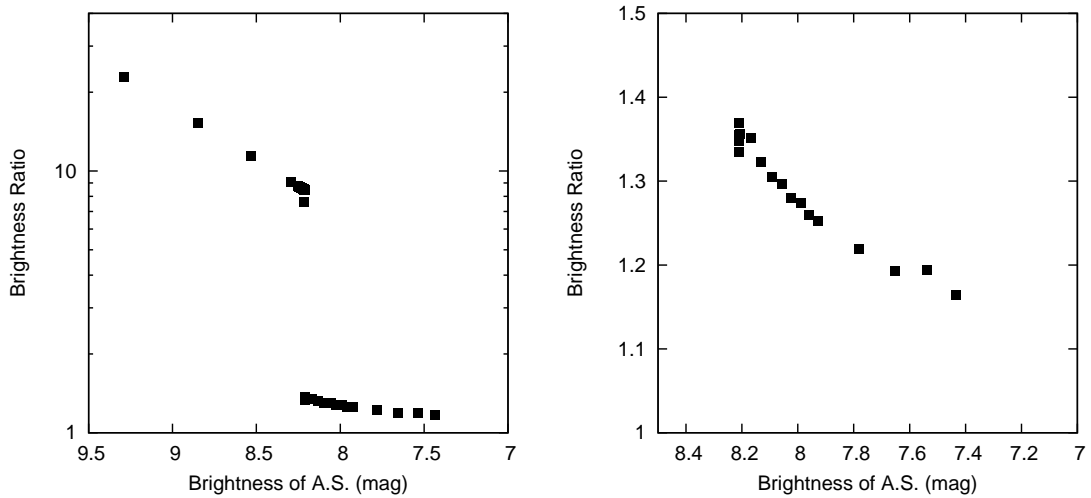
(a) Brightness of the artificial secondary star vs. the brightness ratio of the detected value of the secondary star to the artificial secondary star.

(b) Enlargement of the >8.5 region in the left figure

Figure B.1: *Left* (a): Brightness of the artificial secondary star vs. the brightness ratio of the detected value of the secondary star to the artificial secondary star. *Right* (b): Enlargement of the >8.5 region in the left figure.

The upper limit of the unresolved and undetected actual secondary star is obtained from the brightness of the turning point (~ 8.2 mag) as shown above. In the case of a brighter artificial secondary star, we can detect the embedded artificial source correctly

and vice versa. Finally, we conclude that the upper limit of the unresolved and undetected actual secondary star is >8.34 mag.

However, the brightness of the "actual" secondary star was ignored throughout the resolving process between primary and "artificial" secondary profiles. If the brightness of the actual secondary star affects the resolving process, the stellar profile of the primary star tends toward the side of the actual secondary star to minimize the χ^2. As a result, the stellar profile of the secondary star will approach the location of the primary star to compensate for the remaining brightness of the primary star. Therefore, the estimated value of $\lesssim 8.3$ mag is an overestimate.

List of Publications

Refereed Paper

1. <u>Ito, Y.</u>, Fukagawa, M., Shibai, H., Sumi, T., & Yamamoto, K., 2015, "Study of Infrared Excess from Circumstellar Disks in Binaries with *Spitzer*/IRAC", Publications of the Astronomical Society of Japan, 67, 5, 88, 17

2. Kato, E., Fukagawa, M., Marshall D. Perrin, Shibai, H., <u>Itoh, Y.</u>, & Ootsubo, T., 2011, "Near- and Mid-Infrared Imaging Study of Young Stellar Objects around LkH234", Publications of the Astronomical Society of Japan, 63, 4, 849, 12

3. Fukagawa, M., Tamura, M., Itoh, Y.,4 Oasa, Y., Kudo, T., Hayashi, S., Kato, E., Ootsubo, T., <u>Itoh, Y.</u>, Shibai, H.,& Hayashi, M., 2010, "Subaru Near-Infrared Imaging of Herbig Ae Stars", Publications of the Astronomical Society of Japan, 62, 2, 347, 24

4. Nakashima, A., Shibai, H., Kawada, M., Matsuo, T., Narita, M., Kato, E., Kanoh T., Kohyama, T., Matsumoto, Y., Morishita, H., Watabe, T., Yamamoto, K., Tanabe, M., Kanoh, R., & <u>Itoh Y.</u>, 2011, "Far-Infrared Interferometric Telescope Experiment (FITE): Three-Axis Stabilized Attitude Control System", Transactions of the Japanese Society for Artificial Intelligence, Aerospace Technology Japan, 8, Tm 19

5. Sasaki, A., Shibai, H., Fukagawa, M., Sumi, T., Kanoh, T., Yamamoto, K., <u>Itoh, Y.</u>, Akiyama, N., Terano, A., Aimi, Y., Kuwada, Y., Konishi, M., & Narita, M., 2014,

"Far-Infrared Interferometric Telescope Experiment: Optical Adjustment System",

IEEE Transactions on terahertz science and technology, 4, 2, 179, 4

Conference Proceedings

1. Yamamoto, K., Matsuo, T., McElwain, M., Tamura, M., Morishita, H., Nakashima, A., Shibai, H., Fukagawa, M., Kato, E., Kanoh, T., Itoh, Yusuke, Kaneko, Y., Shimoura, M., Itoh, Yoichi, Funayama, H., & Hashiguchi, T., "Exoplanets and Disks: Their Formation and Diversity", The 2nd Subaru International Conference, Hawaii, 9-12 March 2009. p. 273

2. Sasaki, A., Shibai, H., Sumi, T., Fukagawa, M., Kanoh, T., Yamamoto, K., Itoh, Y., Aimi, Y., Kuwada, Y., Kaneko, Y., Konishi, M., Sai, S., Akiyama, N., & Narita, M., 2012, "Development of new optical adjustment system for FITE (Far-Infrared Interferometric Telescope Experiment)", Optical and Infrared Interferometry III. Proceedings of the SPIE, Volume 8445, 84452Z, 9

3. Shibai, H., Fukagawa, M., Kato, E., Kanoh, T., Kohyama, T., Itoh, Y., Yamamoto, K., Kawada, M., Watabe, T., Nakashima, A., Tanabe, M., Kanoh, R., & Narita, M. "Far-Infrared Interferometric Experiment (FITE): Toward the First Flight", Pathways Towards Habitable Planets, proceedings of a work- shop held 14 to 18 September 2009 in Barcelona, Spain. Edited by Vincent Coud'e du Foresto, Dawn M. G., & Ignasi R. San Francisco: Astronomical Society of the Pacific, p.541

4. Kanoh, T., Shibai, H., Fukagawa, M., Matsuo, T., Kato, E., Itoh, Y., Kawada, M., Watabe, T., Kohyama, T., Matsumoto, Y., Morishita, H., Yamamoto, K., Kanoh, R., Nakashima, A., Tanabe, M., & Narita, M. "De- velopment of the Far-Infrared Interferometric Telescope Experiment", Exo- planets and Disks: Their Formation and Diversity, The 2nd Subaru Interna- tional Conference, Hawaii, 9-12 March 2009. p. 389

5. 芝井 広、住 貴宏、深川美里、叶 哲生、<u>伊藤優佑</u> 、山本広大 、會見有香子 、くわ田嘉大、 小西美穂子、 佐々木彩奈、 秋山直輝、 成田正直、 吉田 哲也、 斉藤芳隆"宇宙遠赤外線干渉計 (FITE) プロジェクト:次回フライト に向けて"、大気球シンポジウム、JAXA/ISAS 、10 月、2012 、p. 32

6. 叶 哲生、 芝井 広、 住 貴宏、深川美里、<u>伊藤優佑</u> 、山本広大 、會見有香子 、金子有紀、 くわ田嘉大、 小西美穂子、 蔡 承亨、 佐々木彩奈、 成田正直、 吉田哲也、 斉藤芳隆、 田村啓輔"気球搭載遠赤外線干渉計 FITE 次回 フライト計画"、大気球シンポジウム、JAXA/ISAS 、10 月、2011 、 p.10

7. 叶 哲生、芝井 広、深川美里、加藤恵理、幸山常仁、<u>伊藤優佑</u> 、山本広大、金子有紀、下浦美那、會見有香子、くわ田嘉大、Dimitrios Kontopoulos 、渡 部豊喜、松尾太郎、川田光伸、成田正直"遠赤外線干渉計 FITE のフライト 計画"、大気球シンポジウム、JAXA/ISAS 、9 月、2010 、p. 96

8. 叶 哲生、芝井 広、松尾太郎、加藤恵理、<u>伊藤優佑</u> 、川田光伸、幸山常仁、松本有加、森下祐乃、狩野良子、田辺光弘、中島亜紗美、山本広大 、渡部豊喜、成田正直、土井靖生"遠赤外線干渉計 FITE の地上試験と観測計画"、大気球 シンポジウム、JAXA/ISAS 、9 月、2008 、p. 61